1 # Atmospheric stability from microwave radiometer

2 # observations for on/offshore wind energy applications

3 Domenico Cimini[1,2], Rémi Gandoin[3], Stephanie Fiedler[4,a], Claudia Acquistapace[5], Andrea

4 Balotti[2], Sabrina Gentile[1,2], Edoardo Geraldi[1], Christine Knist[6], Pauline Martinet[7], Saverio T.

5 Nilo[1], Giandomenico Pace[8], Bernhard Pospichal[5], Filomena Romano[1]

6 [1] CNR-IMAA, C.da S.Loja, Potenza, 85100, Italy

7 [2] CETEMPS, University of L'Aquila, L'Aquila, 67100, Italy

8 [3] C2Wind, Fredericia, 7000, Danmark

9 [4] University of Cologne, Cologne, Germany

10 [5] Institute for Geophysics and Meteorology, University of Cologne, 50969 Cologne, Germany

11 [6] DWD, Meteorological Observatory Lindenberg – Richard Aßmann Observatory, Tauche OT Lindenberg, 15848,

12 Germany

13 [7] CNRM, Université de Toulouse, Météo-France, CNRS, Toulouse, France.

14 [8] ENEA, Observations and Measurements for Environment and Climate Laboratory, Rome, 00123, Italy

15 [a] Now at Institute of Environmental Physics, University Heidelberg, D-69120 Heidelberg, Germany

16

17 *Correspondence to*: Domenico Cimini (domenico.cimini@imaa.cnr.it)

18 **Abstract.** Atmospheric stability controls the evolution of wind turbine wakes, and thus the yield and performance

19 of wind parks. For estimations of wind park power output and for improving analyses of wind park wakes, crucial

20 parameters were found to be profiles of atmospheric temperature and stability metrics. Atmospheric temperature

21 profiles are available from numerical weather prediction (NWP) models or are measured in-situ by balloon-borne

22 sensors, but can also be estimated from the ground using radiometric observations. This paper reviews the stability

23 metrics useful for monitoring wind park performances and provides a quantitative assessment of the value of NWP

24 model data for estimating these metrics. This paper also extends previous work, quantifying the performances of

25 microwave radiometer (MWR) observations to estimate stability metrics from surface-based observations in three

26 climatological conditions (marine, continental, and polar) and with different instrument types, either situated on

27 land or ocean. Two NWP systems (DOWA and NEWA) have been evaluated against temperature profiles

28 measured by offshore met masts in the 30-100 m layer from the surface. Systematic differences are ~0.3-0.5 K,

29 with no clear dependence on the stability class. Conversely, both models show larger random differences in stable

30 than in unstable conditions. Root-mean-square (RMS) differences were within 1 K for DOWA, while it exceeded

31 2 K for NEWA in very stable conditions. For temperature gradients in the 50-100 m vertical layer, the mean

32 absolute error (MAE) was ~3.4-4.2 K/km, with 5.8-8.4 RMS, and 0.7-0.8 correlation. From the six datasets of

33 MWR and radiosonde observations considered here, temperature profiles mostly agree within ~0.5 K near the

34 surface increasing to ~1.5 K at 2 km. Substantial differences are found between MWR performances in retrieving

35 temperature and potential temperature gradients (50-300 m) onshore and offshore. Onshore, potential temperature

36 gradients agree with 2.1-3.4 K/km MAE and 0.7-0.9 correlation. Offshore, both MAE (0.9-1.9 K/km) and

37 correlation (0.3-0.4) are relatively lower, although performances tend to improve using elevation scanning

38 retrievals. Considering all the datasets, reported MAE are 0.9-3.4 K/km, while RMS are 1.2-5.1 K/km. Thus, the

39 uncertainty of MWR for temperature and potential temperature gradients in the 50-300 m vertical layer is ~0.5-

40 4.3 K/km. The relatively lower performances off-shore may be attributed to the training of the inversion method,

41 which may under-represent the peculiar off-shore conditions, and the ship movements, which can impact low-

42 elevation observations. These considerations suggest that appropriate dedicated training and elevation scanning

43 with ship movement compensation may be required for MWR to better catch potential temperature gradients

44 typical of offshore conditions.

45 **1 Introduction**

46 Stability is a characteristic of how a system reacts to small disturbances. If the disturbance is damped, the system

47 is considered to be stable. If the disturbance causes an amplifying response, the system is unstable (Stull, 2017).

48 Atmospheric stability is a measure of the atmospheric state which determines whether air will tend to rise or sink

49 (Spiridonov & Ćurić, 2021). In simple words, a layer is considered as stable when vertical motion is suppressed,

50 and as unstable (or convective), when vertical motion is enhanced (Stull, 2012). Stability conditions are often

51 mainly driven by the balance between momentum and heat fluxes close to the surface and can be described by

52 similarity laws (Gryning er al, 2007). However, there are conditions under which the characterisation of stability

53 requires detailed information of the atmospheric boundary layer (ABL) across height, for instance when warm air

54 is advected aloft over a colder surface. In fact, the buoyancy (B), that is the acceleration of an air parcel after a

55 certain displacement over height (Δz) is proportional to the atmospheric potential temperature (θ) and its vertical

56 gradient ($\frac{d\theta}{dz}$), as:

57 $$B = -\frac{g\Delta z}{\theta}\frac{d\theta}{dz}$$

58 (1)

59 where g is the gravitational acceleration and θ is defined through air temperature (T) and pressure (P) as (Stull,

60 2012):

61 $$\theta = T(\frac{P_0}{P})^{R/c_p}$$

62 (2)

63 with P_0 as reference pressure (e.g., 1000 hPa), and R/c_p the ratio between the gas constant and the specific heat

64 capacity at a constant pressure for air. If the parcel is moved up ($\Delta z > 0$) and $\frac{d\theta}{dz} < 0$, the buoyancy tends to lift the

65 parcel further ($B > 0$, instability); conversely, if $\frac{d\theta}{dz} > 0$ the buoyancy moves the parcel back towards its original

Atmospheric
Measurement
Techniques
Discussions

EGU

Open Access

66   location ($B<0$, stability). Atmospheric stability is relevant for meteorological processes and applications,
67   including air quality, and renewable energy yield. In particular, atmospheric stability is relevant for the prediction
68   of vertical wind shear (larger during stable conditions) and turbulence (larger during unstable conditions). Wind
69   turbine rotors span a relatively large range of elevations (between approx 23 to 250 m ASL for a modern turbine),
70   so the thermodynamic conditions in the lowest 300 m are the most relevant for this application. In particular,
71   atmospheric stability has a major impact on the characteristics of wind turbine wakes and thus on the yield and
72   performance of offshore wind parks (Hansen et al, 2012). However, simple approaches for defining stability, e.g.,
73   using surface layer stability metrics such as the Obukhov length (Obukhov, 1971; Foken, 2006) or the temperature
74   difference between the sea surface and the atmosphere at one particular altitude, are not always suitable for
75   describing stability conditions and wake development. For the estimation of wind park power output and for
76   improving analyses of offshore wind park wakes, atmospheric temperature profiles and stability metrics were
77   found to be crucial parameters. In fact, improved characterisation of wind farm output can be produced if the
78   boundary layer stability is considered, indicating the need for temperature measurements at separate heights
79   (Vanderwende and Lundquist, 2012). Different power curves shall be calculated for different stability conditions,
80   leading to more accurate and reliable performances of energy production calculations (St. Martin et al., 2016).
81   For example, for a wind energy farm in a coastal region, Perez et al. (2023) reported that unstable atmospheric
82   conditions deliver up to 8% more power than stable conditions, while neutral conditions deliver up to 9% more
83   energy than stable conditions. As a small percent difference leads to a large deviation in cost for both operators
84   and manufacturers, calculating different power curves for different atmospheric conditions lowers the financial
85   risks for both operators and manufacturers (St. Martin et al., 2016). In particular, temperature inversions are
86   important, which may occur above, below, and within the wind turbine rotor area. These conditions would affect
87   the wake development in different ways, e.g., (*i*) decoupling the wake from the surface or (*ii*) preventing the wake
88   vertical spreading for inversions below/above the rotor area, respectively (Platis et al., 2020).
89   Atmospheric temperature profiles can be measured in situ by sensors located on instrumented towers, drones, and
90   balloons. Instrumented towers have the advantage of providing temperature profiles nearly continuously in time.
91   However, the costs for their installation and maintenance are quite demanding, and particularly impractical on
92   offshore platforms, resulting in limited deployment (up to ~100 m height, to our knowledge). Also drones have
93   limited range in altitude with about 120 m in US and Europe, unless special waiver by corresponding aviation
94   safety agencies (Pinto et al., 2021; Hervo et al., 2023), and in addition their use requires attended service.
95   Conversely, sondes attached to balloons, referred to as radiosondes, can nowadays be launched by automatic
96   stations (Madonna et al., 2021) and usually reach elevations well above the ABL (25 km altitude or more). Each
97   radiosonde measures one instantaneous and vertically high-resolution profile of atmospheric temperature,
98   humidity, wind speed and direction. However, the cost of a radiosonde launch is such that they are typically

99   launched once or twice a day, except at major atmospheric observatories run by meteorological services that have

100   up to four radiosondes per day or during field campaigns with a radiosondes program to meet research needs.

101   Remote sensing technology has the potential to overcome some of the limits of in-situ measurements. Ground-

102   based measurements of atmospheric temperature and humidity profiles are possible using microwave radiometers

103   (MWR, Cimini et al., 2006), infrared spectrometers (IRS, Feltz et al., 2003), and radio-acoustic sounding systems

104   (RASS, Bianco et al., 2017). These remote sensing systems provide unattended operations and high temporal

105   resolution (order of minutes) measurements that are used for a range of applications, including operational

106   meteorology (Cimini et al., 2015; Shrestha et al., 2021), atmospheric study processes (Martinet et al., 2017;

107   Martinet et al., 2020; Wagner et al., 2022), and weather forecast (Caumont et al., 2016; Lin et al., 2023; Cao et

108   al., 2023). Conversely, atmospheric thermodynamic profilers have not been exploited extensively for wind energy

109   applications, despite the general recognition of the importance of temperature profiles and atmospheric stability

110   regimes for the characterization of wind energy production (Vanderwende and Lundquist, 2012; St. Martin et al.,

111   2016; Perez et al., 2023). Ongoing efforts in this direction include the series of on/offshore field campaigns

112   performed within the Wind Forecast Improvement Projects (WFIP, Wilczak et al., 2015; Shaw et al., 2019;

113   Wilczak et al., 2019). Although the uncertainty requirements for atmospheric stability measurements to serve

114   wind energy applications have not been assessed yet, it is useful to assess the accuracy currently achievable by

115   remote sensing thermodynamic profilers. To this end, Bianco et al. (2017) assessed the accuracy of MWR and

116   RASS in light of onshore wind energy applications. This study proved that these remote-sensing instruments can

117   provide accurate information on atmospheric stability conditions in the ABL, with 0.87-0.95 correlation between

118   temperature lapse rate in the 50-300 m range as measured by a MWR and tower sensors (note that here and

119   throughout this paper correlation is evaluated with the Pearson's linear correlation coefficient, not to be confused

120   with the determination coefficient R^2 used elsewhere, e.g., by Bianco et al., 2017). Combining this with the need

121   for temperature gradients for onshore and offshore wind energy (e.g., Platis et al. 2020; Perez et al., 2023), it

122   seems natural to extend the investigation of MWR performances to other environmental conditions.

123   Building on these premises, the Carbon Trust Offshore Wind Accelerator (OWA) funded the Radiometry and

124   Atmospheric Profiling (RAP) scoping study. RAP aimed at assessing existing MWR technology and its

125   performances for atmospheric profiling and stability measurements. This paper presents the main outcomes of the

126   RAP project. Section 2 presents a review of capabilities from numerical weather prediction (NWP) modelling

127   systems (hereafter: NWP models), which represent the default option in the absence of measurement data. Section

128   3 briefly introduces MWR technology currently available and the datasets exploited for this analysis. Section 4

129   presents the validation of temperature gradients measured by MWR units with respect to reference radiosonde

130   data. Section 5 presents a summary, conclusions, and plans for dedicated onshore and offshore field campaigns.

131

Atmospheric
Measurement
Techniques
Discussions

132 **2 Validity assessment of NWP datasets**

133 As part of the RAP project, the validity of NWP models for assessing atmospheric stability for the purposes of

134 offshore wind engineering was investigated. The following model datasets were used: (*i*) ERA5 from the ECMWF

135 (Hersbach et al., 2020) obtained via the Copernicus Climate Change Service (C3S, 2021), (*ii*) the New European

136 Wind Atlas (Lundtang Petersen, 2014; NEWA, 2021), and (*iii*) the Dutch Offshore Wind Atlas (Wijnant et al.,

137 2019; DOWA, 2021). NEWA and DOWA have been produced using two different mesoscale NWP models, and

138 both use ERA5 as input. Measurement data came from the FINO1, FINO2 and FINO3 met masts, via the German

139 Federal Maritime and Hydrographic Agency (https://www.bsh.de/EN/), and from the IJmuiden met mast as well

140 as floating lidar measurements in the Southern North Sea, via The Netherlands Enterprise Agency

141 (https://english.rvo.nl/).

142 **2.1 Surface stability metrics**

143 For characterising atmospheric stability in the surface layer, pre-existing validation studies have been used (i.e.,

144 Peña et al., 2008; Peña and Hahmann, 2011; Sathe et al, 2011). In order to validate the wind speed profile

145 analytical models proposed originally by Gryning et al. (2007), the focus was set on the Obukhov length (L):

146 $$L = \frac{-u_{*0}^3}{\kappa(g/T)\overline{w'T'}_0}$$

147 (3)

148 where u_{*0} and $\overline{w'T'}_0$ are respectively the friction velocity and kinematic heat flux at the surface, κ is the von

149 Karman constant (≈ 0.4), T the temperature, and g/T the buoyancy parameter. The NEWA Obukhov length time

150 series are readily available, while for ERA5 it was derived from the single levels datasets using two methods:

151 firstly using the turbulent fluxes, and secondly computing the bulk Richardson number (Ri_b) from sea surface

152 temperature, air temperature and wind speed at 2 and 10 m ASL, respectively, and relating Ri_b to the

153 dimensionless stability parameter z/L (where z is the height above ground level), i.e.:

154 $$\frac{z}{L} = C_1 Ri_b$$

155 (4)

156 $$\frac{z}{L} = \frac{C_2 Ri_b}{1 - C_3 Ri_b}$$

157 (5)

158 for unstable and stable conditions, respectively (Peña et al., 2008). The values of C constants are adopted from

159 Grachev and Fairall (1997): $C_1 = C_2 \approx 10$ and $C_3 \approx 5$. Similarly, the Obukhov length was derived from

160 measurements, i.e., the HKZA floating lidar dataset (de Montera et al., 2022) using the same method (via the bulk

161 Richardson number) mentioned above for ERA5: the 10 m ASL wind speed was derived from the 4 m ASL sonic

162 anemometer and three smallest lidar elevations at 20, 30 and 50 m ASL. The results from the models and

163 measurements are compared in Figure 1. Overall, the best match between model data and measurements is

164 observed for ERA5 datasets computed using the fluxes for unstable conditions (i.e. $10/L < -0.03$). For stable

165 conditions ($10/L > 0.03$), the best match is observed when using the bulk Richardson number-derived ERA5

166 time series. These results confirm that when the main drivers of atmospheric stability (i.e., air- and surface

167 temperature difference, wind speed) are correctly characterised by the bulk formulations used in NWP models,

168 the modelled Obukhov length time series compare well - in an average sense - to those derived from

169 measurements. This implies that such results are hardly generalisable, that is: the user of model datasets should

170 check, across the region of interest, the validity of these key variables. This can for instance be done using buoy

171 measurements, where available.

172
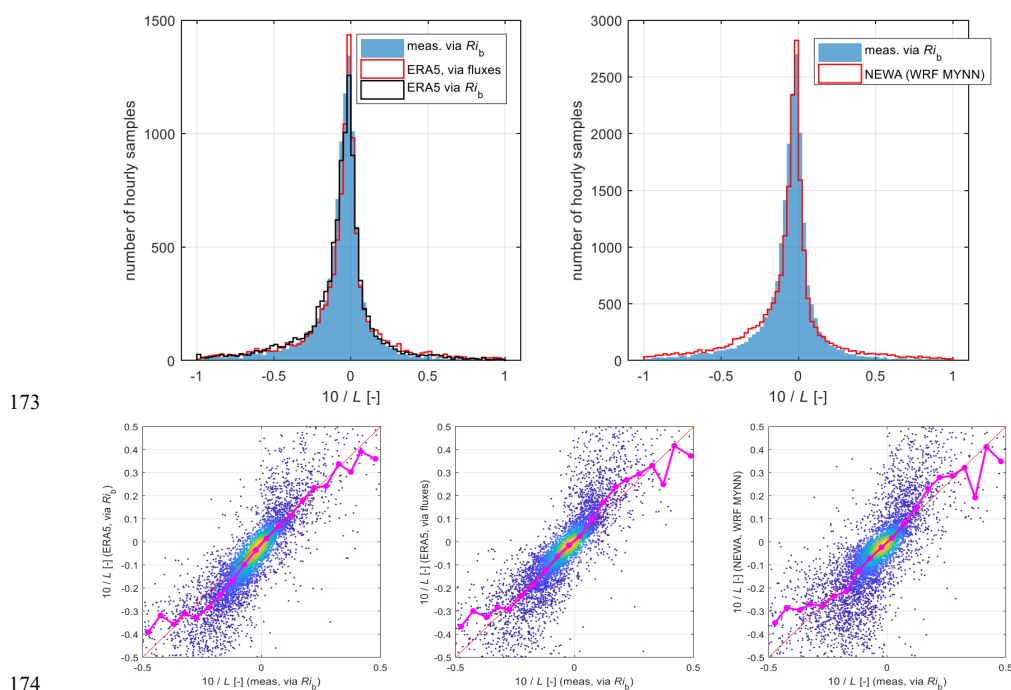
173

174

175 **Figure 1.** Top: Histograms of the dimensionless stability parameter z/L (where $z = 10$ m MSL and L is the Obukhov length).

176 Bottom: Comparison between measured (Ri_b-based) values and modelled values (see y-axes) of z / L, at the HKZA FLS

177 location, and using ERA5 and NEWA model data, for 10 m MSL wind speeds larger than 10 m/s. The measurements have

178 been averaged to hourly values.

179

180   Practitioners are primarily interested in how these modelled Obukhov length time series can improve wind-related
181   analyses. Two examples are provided in Figure 2 and Figure 3; they both use ERA5-derived Obukhov length time
182   series derived from fluxes. The first example focuses on turbulence intensities (TI), i.e., the ratio of the root-mean-
183   square of the eddy velocity to the mean wind speed, and mean horizontal wind speed (WS). Figure 2 shows how
184   measured TI and WS spectra vary with the atmospheric stability class indicated by the modelled Obukhov length:
185   as classically reported in the literature, turbulence intensities are smaller in stable ($z/L \geq \sim 0.1$) than in unstable
186   ($z/L \leq \sim -0.1$) conditions. In addition, the WS spectra progressively increase as conditions shift from stable to
187   neutral to unstable. The second example shows how the set of analytical expressions proposed by Gryning et al.
188   (2007) and the method outlined in Peña et al. (2008) compare with simpler, surface-layer expressions, such as the
189   Monin-Obukhov Similarity Theory (MOST). Note that the expressions from Gryning et al. (2007) basically form
190   an extension of the MOST above the surface layer (SL). Figure 3 confirms that MOST predicts well the wind
191   speed profile in neutral and unstable conditions, while it significantly overpredicts the measurements above 30 m
192   in very stable conditions. This is due to the influence of other scaling parameters such as the boundary-layer
193   height, which is not accounted for in surface-layer scaling. Figure 3 also corroborates the findings from Peña et
194   al. (2008), showing that accounting for the effect of the boundary-layer height in stable conditions is essential to
195   better capture the wind speed above 30 m with respect to MOST, correcting the overprediction up to the boundary-
196   layer height. This improvement is due to better modelling of characteristic length scales of the turbulent eddies
197   for the ABL layers located above the surface layer, especially in stable conditions when the surface layer is very
198   shallow (i.e., less than 100 m in depth).
199

200

201
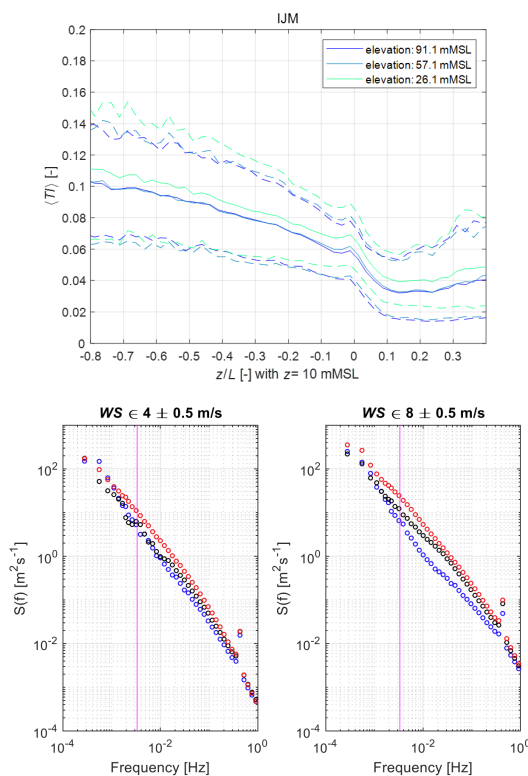
Figure 2. Left: Dependence of the turbulence intensity (TI) on the atmospheric stability, for the IJmuiden met mast dataset. Here, the stability is expressed on the x-axis using the Monin-Obukhov length L and the ratio z/L with z = 10 m MSL. Different line colours indicate TI measured at different measurement heights. The full lines are mean values, the dashed lines are 10- and 90-percent quantiles. Two right plots: mean hourly power spectra measured at the top of the IJmuiden met mast (91.1 m MSL), for various stability classes (blue: stable, red: unstable, black: neutral), and two wind speed bins (8 and 12 m/s, respectively). The vertical magenta lines indicate 3.3 mHz frequency, corresponding to 5-minute interval (1/300s).

208
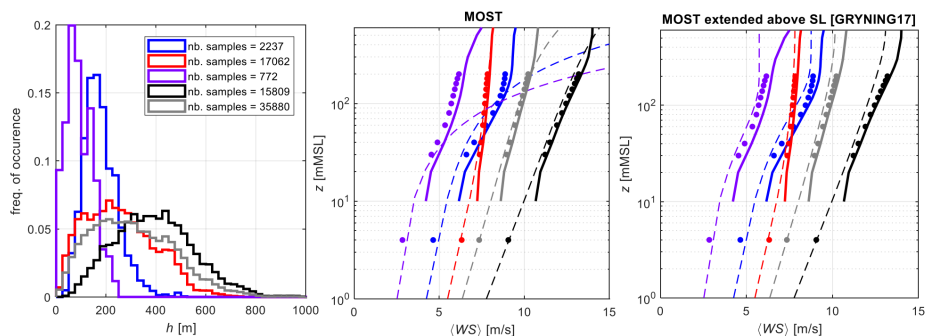
Figure 3. Left: histograms of the boundary layer height (h) as defined in Gryning et al. (2007). Different colours correspond to different stability classes: purple is very stable, blue is stable, red is unstable, black is near-neutral and neutral, and grey shows all data. Center: profiles of wind speed; dots are measurements from the HKZA floating lidar, full lines are from the DOWA dataset, while the dashed lines are from the MOST. Right: Same as in the centre, but for the MOST SL-extended model from Gryning et al. (2007).

It is concluded that for offshore areas during cases when the main drivers of atmospheric stability are correctly characterised by NWP models, these results can provide wind energy practitioners with valid (in an average sense) Obukhov length time series which can be used for a range of analyses, including estimates of turbulence and wind shear. However, in specific cases, the simulated profiles need to be carefully assessed with observations, since the wind speed profiles and hence the vertical shear and associated turbulence characterization may not be sufficiently accurate. This is a long-standing limitation especially for stably stratified boundary layers (Sandu et al., 2013).

2.2 Temperature profiles across the ABL

The validity of NWP model data to characterise the air temperature profile in different stability conditions was assessed using air temperature measurements from tower sensors located approximately from 30 to 100 m ASL. Only DOWA and NEWA data were available at the same elevations as the measurements, while the ERA5 provides only few samples at these elevations. Tower measurements and model data have been divided in five classes of stability conditions: very unstable ($10/L < -0.1$), unstable ($-0.1 \leq 10/L < -0.05$), neutral ($-0.05 \leq 10/L < 0.05$), stable ($0.05 \leq 10/L < 0.1$), and very stable ($10/L \geq 0.2$). Figure 4 shows mean temperature profiles from measurements and model data and their mean and RMS differences in those five classes. DOWA and NEWA models give similar results, providing temperature profiles close to measurements in average for all stability conditions. Mean differences range from ~0.3 to 0.5 K, with no clear pattern with respect to stability class. Conversely, both DOWA and NEWA models show increased RMS in stable conditions with respect to unstable conditions, with minimum RMS in neutral conditions. DOWA seems to perform better (RMS within 1

235   K throughout the 30-100 m range) than NEWA, especially in very stable conditions (RMS up to 2.2 K). To

236   measure the NWP overall performances in modelling atmospheric stability, one may look at the performances in

237   predicting the vertical gradient of temperature ($\frac{dT}{dz}$). In fact, recalling Eq.(1), stability directly depends upon the

238   vertical gradient of potential temperature ($\frac{d\theta}{dz}$), which is well correlated with $\frac{dT}{dz}$. This is shown in Figure 5,

239   reporting the scatter of $\frac{dT}{dz}$ between 50 and 100 m ASL as modelled by the DOWA and NEWA datasets and

240   measured by the tower sensors at the FINO1 and FINO3 platforms. Data points are quite scattered, with model

241   data covering a range (~100 K/km) lower than measurements (~200 K/km). As for the temperature profiles, the

242   DOWA dataset performs better than the NEWA, in terms of mean absolute error (MAE, 3.4 to 4.0 K/km for

243   DOWA, 3.5 to 4.2 K/km for NEWA), RMS (5.8 to 7.3 K/km for DOWA, 6.4 to 8.4 K/km for NEWA), and

244   correlation (0.77 to 0.80 for DOWA, 0.70 to 0.71 for NEWA).

245

246

247
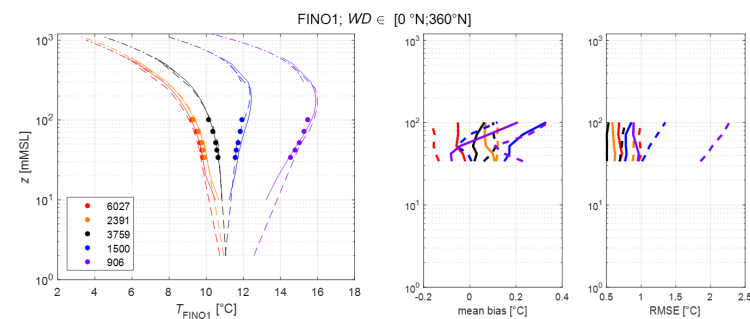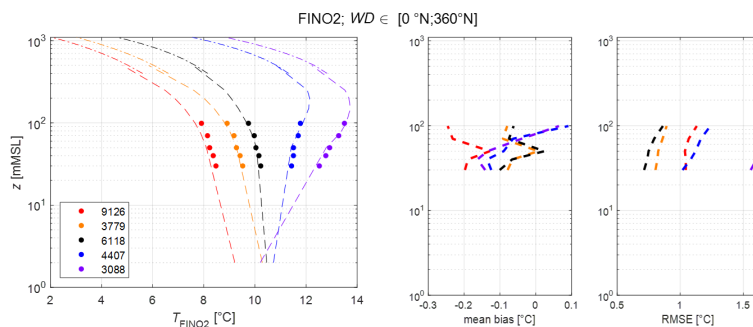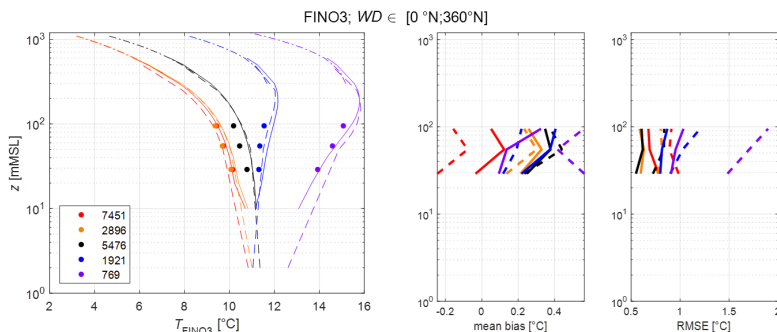
Figure 4. Left: Temperature profiles from measurements (dots) and model data (full lines: DOWA, dashed lines: NEWA, dash dotted lines: ERA5) at three measurement locations: FINO1 (top), FINO2 (middle), and FINO3 (bottom). Center: mean model minus measurement temperature differences. Right: temperature RMS differences. Colours indicate stability class: very unstable (red), near-neutral and unstable (orange), neutral (black), near-neutral and stable (blue) and very stable (purple). DOWA data are not shown in the middle panels as DOWA's domain does not cover FINO2 area.
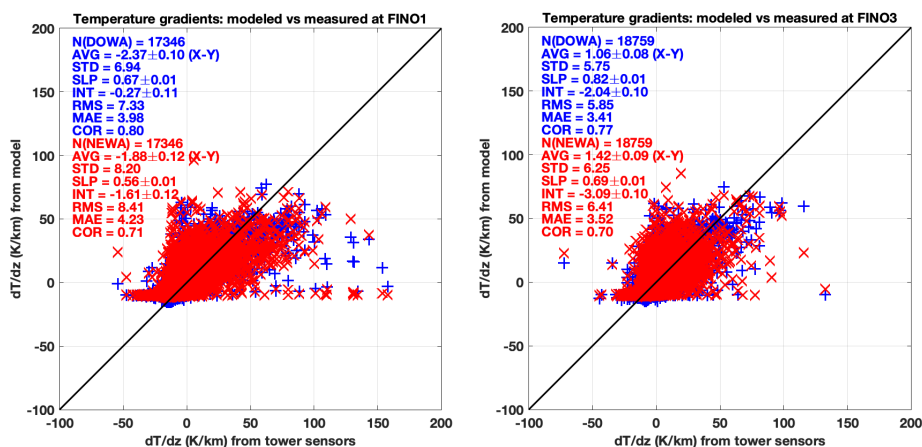
Figure 5. Scatter plots of atmospheric temperature lapse rate (~50–100 m) from tower measurements at FINO1 (left) and FINO3 (right) and model data (DOWA: blue crosses; NEWA: red Xs). N indicates the sample size, AVG the average difference (± 95% confidence interval), STD the standard deviation, SLP and INT the slope and intercept of a linear fit (± 95% confidence interval), RMS the root-mean-square, MAE the mean absolute error, and COR the correlation coefficient R. Units for AVG, STD, RMS, and MAE are in K/km.

Atmospheric
Measurement
Techniques
Discussions
Open Access
EGU

262 **2.3 Conditions for difficult stability characterization**

263 The results from Sections 2.1 and 2.2 show that surface stability metric can suffice for a number of analyses,

264 where the model results are validated in an average sense (mean- wind speed or turbulence intensity, for instance).

265 Other purposes require investigating short-lasted events, characterised by different stability conditions at the

266 surface compared with higher elevations. This is for instance the case for the interpretation of wind maps from

267 synthetic aperture radar (SAR) observations or in-situ profile measurements from uncrewed aircraft systems

268 (UAS) as in, e.g., the WInd PArk Far Fields (WIPAFF) project where both of these measurement types were used

269 (Platis et al., 2020). An illustrative example is provided in Figure 6, where SAR-derived 10 mASL wind speeds

270 are plotted over an area covering the Belgian offshore wind farm cluster. Figure 6 also shows the SAR-derived

271 wind speeds across the cluster, as well as mean wind speed profiles measured at the BWFZ01 location together

272 with model data (which do not include the wind farms), and the vertical temperature profiles from ERA5 and

273 DOWA NWP models. The situation seems to correspond, according to the DOWA and ERA5 data, to neutral

274 conditions at the surface, with a stable inversion cap at ~150 mASL. The SAR-derived winds show that the wakes

275 from the Belgian cluster extend over a long distance (tens of kilometres), and the reason is likely the very steep

276 gradient in potential temperature (27 K/km between 120 and 150 mMSL), capping the lowest (neutral in this case)

277 layer of the atmosphere. This at least what the DOWA model indicates, as there are no air temperature

278 measurements which can confirm this. In any case, the observed, and modelled surface stability metrics indicate

279 unstable to neutral conditions at the surface; this would be an incorrect way to characterise the wind flow

280 controlling the wind farm wake, which is very likely located in a stable layer.

281
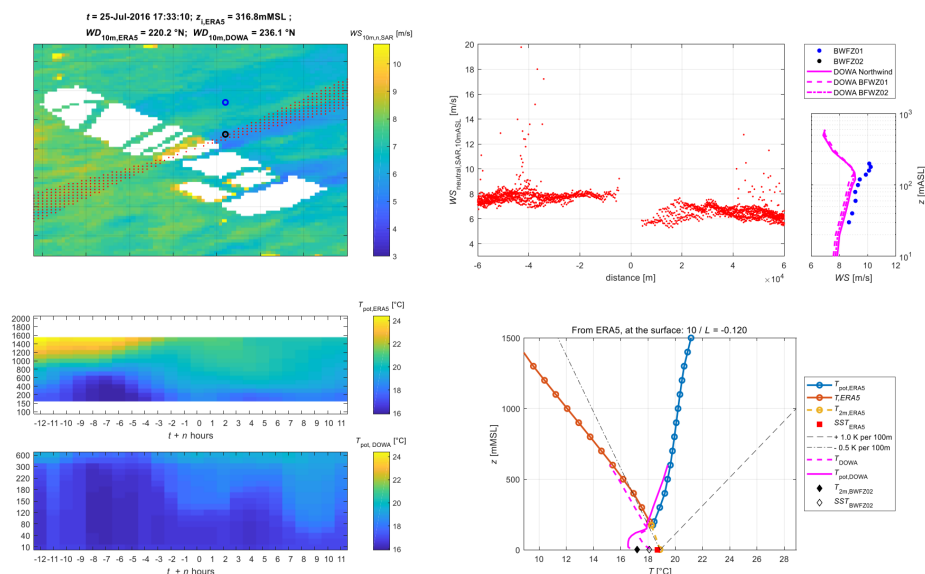
Figure 6. Example of a long wake episode across an offshore wind cluster in the Belgian North Sea on July 25th 2016. Clockwise from top-left: (a) SAR-derived 10 mASL wind speeds mapped over an area covering the Belgian offshore wind farm cluster (white areas indicate lease areas; red dots indicates the location of wind speeds reported in panel (b); blue circles indicate the location of two floating lidars, BWF01 and BWF02). (b) SAR-derived wind speeds crossing the offshore cluster (from -60 to 60 km distance, where 0 indicates the centre of the cluster). (c) Wind speed profiles from floating lidar measurements and DOWA model at the two downwind sites shown in panel (a). (d) Temperature and potential temperature profiles from NWP models ERA5 and DOWA at the time of the SAR image. The red square indicates the sea surface temperature (SST) from ERA5, while the diamonds indicate SST (empty) and 2-m temperature (filled) from measurements at BWFZ02. Dashed and dot-dashed grey lines indicate +1K and -0.5K per 100 m gradients. The estimated Obukhov length at the surface is reported, indicating unstable to neutral conditions (10/L=-0.120). (e) Vertical temperature profiles from NWP models from 10 to 600 m (DOWA) and 160 to 1600 m (ERA5) in the 12 hours before and after the SAR image.

To further investigate the uncertainty associated with the NWP models for such transient flow events, air temperature data from the NEWA dataset have been compared with measurements from the WIPAFF project (Bärfuss et al, 2019). For each of the WIPAFF flights, the NEWA air temperature data have been spatially and temporally interpolated at the UAS locations (down-sampled, from the original dataset). Figures such as Figure 7 have been produced for each WIPAFF flight and are provided as supplement material. The plots indicate the need for temperature measurements above 100 mMSL, as they suggest that such measurements could help understand whether such important phenomena for wind farm wake modelling as temperature inversions are well captured

by mesoscale models when they occur above 100 mMSL, where measurements are often not available. Such a
need may be satisfied by nearly continuous observations from a microwave radiometer profiler. The ability to
profile atmospheric temperature continuously within the first 2 km and to provide potential temperature gradients
in the vertical range of wind turbine rotors is assessed in the next Section.
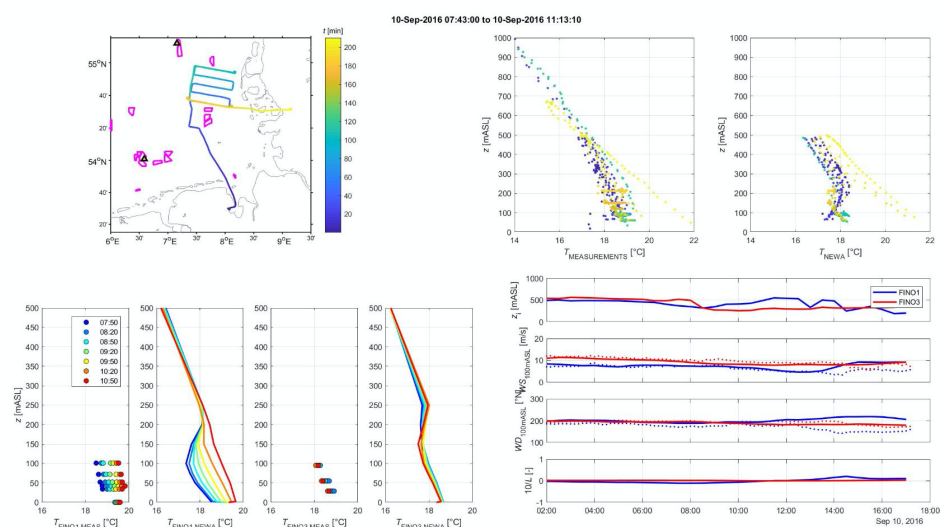
Figure 7: Comparison of temperature from in-situ measurements and NEWA model data over the German Bight from the WIPAFF campaign on September 10, 2016. Clockwise from top-left: (a) Flight path with the location of existing wind farms (indicated by magenta shapes) and the two met masts at FINO1 and FINO3 locations (black triangles in the southern and northern part of the map, respectively). Line colour indicates time from flight start. (b) Comparison of temperature profiles from in-situ measurements (flights) and NEWA model datasets (color-coded according to the corresponding flight time in panel (a)). (c) Time series of ABL height, wind speed and direction at 100 m, and Obukhov length at surface provided by ERA5 during the flight time period (blue line: FINO1; red line: FINO2). Wind speed and direction measured at 100 m from met masts are also shown (dotted lines). (d) Comparison between temperature profiles from in-site measurements (met masts) and NEWA model data during the flight time period (color-coded according to the corresponding flight time in panel (a)).

317

3 Datasets and methodology

3.1 Microwave radiometer technology

Microwave radiometry is a passive technique that has been used for several decades to observe atmospheric thermodynamic profiles. Ground-based microwave radiometers (MWR) are instruments measuring the down-welling natural thermal emission from the Earth's atmosphere, conveniently expressed in terms of brightness temperature (T_B), which is inverted into atmospheric thermodynamic products using statistical regression, neural network, or optimal estimation (Cimini et al., 2006). The ability to retrieve atmospheric variables depends upon the number and spectral allocation of the frequency channels at which the MWR measures T_B. The ability to retrieve atmospheric temperature profiles is related to thermal emission from oxygen, a well-stratified gas whose concentration is nearly constant in space, time, and height. Thus, radiation emitted by oxygen depends primarily on temperature, and T_B measurements at channel frequencies exhibiting strong oxygen emission are highly correlated with atmospheric temperature. This is the case for the strong oxygen absorption complex at 50-70 GHz, which is well established and widely used for probing atmospheric temperature from the ground as well as from space. At channels in the centre of the absorption band (~60 GHz) the atmosphere is highly opaque and the observed T_B carries information on the temperature near the instrument. Conversely, at channels away from the centre (e.g., 50-55 GHz), the atmosphere is less opaque and the signal systematically stems from atmospheric layers further from the instrument. Thus, vertical temperature profiles of the lower atmosphere are estimated from observations corresponding to different atmospheric absorption. The required information content can be obtained by multi-channel observations in the 50-60 GHz range but also by single-channel observations at several elevation angles. Similarly, observations at 22-32 GHz provide information on atmospheric humidity and column integrated water vapour (IWV) and liquid water path (LWP) simultaneously. Thus, ground-based MWR units operating in both the 22-32 GHz and 50-60 GHz bands are sometimes called MWR profilers (MWRP) and are commonly used to estimate atmospheric temperature and humidity profiles (Rüfenacht et al., 2021; Shrestha et al. 2021). A handful of MWR profiling types are currently available as off-the-shelf commercial products. Also a few research prototypes have been developed or are currently under development. For the scope of RAP, i.e. atmospheric profiling related to stability, only the temperature profilers and the MWRP are of interest. In our survey, we found only five commercially-available MWR products corresponding to these characteristics. These are listed in Table 1, together with their main characteristics. In addition, a prototype for marine deployment on a floating buoy or offshore platform is considered, though not commercially available yet.

347

Table 1: Main features of MWR types identified for potential interest for the atmospheric profiling related to stability (listed in alphabetical order of manufacturer). An estimate of the technology readiness level (TRL) is also shown. TLR 4-5 indicates

350 technology validated in the laboratory and relevant environment; TLR 9 indicates actual system proven in the operational

351 environment.

Manufacturer	MWR name	Atmospheric retrievals	Range (km)	Type	TRL
Attex	MTP-5	Temperature profile	<1 km	Single-channel; continuous elevation scanning.	9
BEST	MPR	Temperature profile IWV, LWP	<10 km	Multi-channel (2 polarisation); continuous elevation scanning.	4-5
Radiometrics	MP-2500A	Temperature profile	<10 km	Multi-channel; elevation scanning; optional azimuthal scanning.	9
Radiometrics	MP-3000A	Temperature profile Humidity profile IWV, LWP	<10 km	Multi-channel; elevation scanning; optional azimuthal scanning.	9
RPG	HATPRO	Temperature profile Humidity profile IWV, LWP	<10 km	Multi-channel; elevation scanning; optional azimuthal scanning.	9
RPG	TEMPRO	Temperature profile	<10 km	Multi-channel; elevation scanning; optional azimuthal scanning.	9

352

353 For temperature profiles most of the information and the resolution resides in the first 2 km. Different methods

354 are used to quantify the vertical resolution of radiometric profiling. Using the inter-level covariance, Cimini et al.

355 (2006) reported that the vertical resolution of retrieved temperature profiles in the 0-3 km vertical range decreases

356 linearly with height z as approximately $\sim 0.44 \cdot z$. Measurements at different elevation angles enhance the vertical

357 resolution of ABL temperature profile retrievals. Thus, elevation-angle scanning capability is often available in

358 MWRP units.

359 MWR units operate in all weather conditions. However, retrieved products may be unrealistic in case of water

360 accumulation over the radome, which produces additional microwave radiation not related with the atmospheric

361 state. A number of solutions for detecting and mitigating dew and precipitation effects are used in current MWR

Atmospheric
Measurement
Techniques
Discussions

362 instruments, including rain sensor, hydrophobic coating, tangent blower, heaters, shutter, and side-views. These

363 mitigation solutions effectively avoid water accumulation on the radome or mitigate its effect on the retrieved

364 products in most of the cases. However, chances are that mitigation solutions fail during intense rainfall or

365 snowfall. Proper maintenance (cleaning and replacing) of the radome helps in reducing cases of precipitation

366 mitigation failures. This requires regular services and replacement (e.g., every few months, depending upon

367 environment conditions). Off-shore conditions (high likelihood of sea sprays) may require more frequent

368 intervention.

369 A thorough assessment of MWR ability to provide atmospheric stability is given in Bianco et al. (2017),

370 specifically addressing wind energy applications. They report the outcome of a remote-sensing system evaluation

371 study, called XPIA (eXperimental Planetary boundary layer Instrument Assessment), held in spring 2015 at

372 NOAA's Boulder Atmospheric Observatory (BAO; Wolfe & Lataitis, 2018). BAO is equipped with a 300 m tower

373 mounting temperature and relative humidity sensors at six levels (50, 100, 150, 200, 250, and 300 m). In addition,

374 some 60 radiosondes were launched during the XPIA 2-month period. Two MWR of the same type (Radiometrics

375 MP3000-A, see Table 1) were deployed. To assess the MWR's ability to estimate atmospheric stability, they

376 compared MWR with tower measurements, analysing the vertical gradient of temperature T and potential

377 temperature θ for 50-300 m. For T gradient (dT/dz), they reported mean absolute error (MAE) within 2.1 K/km

378 and bias within 0.1 K/km, with 0.95 correlation. For potential temperature gradient ($d\theta/dz$), they reported MAE

379 within 2.2 K/km and bias within 0.1 K/km, with 0.95 correlation. They also investigated gradients for thinner

380 atmospheric layers (i.e., 50-150, 50-200, 50-250 m), reporting performances slightly degraded with respect to the

381 50-300 m layer. They also investigated the temperature profiling performances during rainy and non-rainy periods,

382 reporting no significant difference. They concluded that MWR can be useful for understanding conditions leading

383 to strong vertical windshear or turbulence, which can affect the loads on rotors. The next section extends the

384 results of Bianco et al. (2017) to other measurement conditions, including onshore and offshore.

385

386 **3.2 Datasets**

387 The results of Bianco et al. (2017) are obtained in a continental high-elevation site (Eire, Colorado, USA, ~1500

388 m altitude), using one of the MWR types in Table 1. This section aims to extend the analysis of Bianco et al.

389 (2017) to other environmental conditions and to the most common commercially available MWR system types in

390 Table 1. Thus, we identified datasets that would fit the purpose of validating MWR retrievals in different

391 environments, possibly both for onshore and offshore deployments. Several research and operational networks

392 operate onshore MWR continuously and provide open access to their data, e.g., the U.S. Atmospheric Radiation

393 Measurement (ARM, www.arm.gov) programme (Cadeddu et al., 2013), the European E-PROFILE programme

394 (Rüfenacht et., 2021), the New York State Mesonet (Shrestha et al., 2021). However, none of these MWR sites

Atmospheric
Measurement
Techniques
Discussions

395   are equipped with a 300 m tower as in BAO. Thus, the validation of MWR retrievals is here performed against in

396   situ measurements performed by balloon-borne radiosonde temperature sensors. Radiosondes are launched

397   routinely at a limited number of MWR sites and usually extend well above the altitude range relevant to wind

398   energy applications. Thus, we selected four datasets of colocated MWR and radiosonde observations taken at four

399   onshore sites including marine, continental, and Arctic environments: Graciosa island (Azores Archipelago,

400   Portugal), Saint-Symphorien (France), Lindenberg (Germany), and Pituffik (Greenland). Conversely, offshore

401   MWR deployments are rare, despite their potential for wind energy industry. To our knowledge, the only MWR

402   deployment on a fixed offshore platform was in the framework of the Offshore Boundary-Layer EXperiment at

403   FINO1 (OBLEX-F1, https://oblo.w.uib.no/activities/the-oblex-f1-measurment-campaign/), which took place

404   from May 2015 to September 2016 at the German wind energy research platform FINO1, in close vicinity to the

405   offshore wind park Alpha Ventus in the North Sea. The main purpose of the campaign was to improve

406   understanding of the marine boundary-layer in the vicinity of an offshore wind farm with respect to wind speed

407   profiles, atmospheric stability regimes, single turbine and wind farm wake propagation effects, under real offshore

408   conditions. To complement the resident instrumentation at the FINO1, several instruments were installed for the

409   campaign, including sonic anemometers, scanning wind lidars, and a MWR. The MWR (RPG HATPRO, see

410   Table 1) was deployed on the upper deck, at the base of the 100-m meteorological instrumented tower. However,

411   this dataset is not open access and the closest radiosondes are launched more than 50 km away from the coastal

412   site on the Norderney island (Germany). Conversely, colocated offshore MWR and radiosonde observations are

413   available from ship-based deployments, such as those performed in the framework of oceanic field experiments

414   (e.g., Bony et al., 2017). Thus, we selected two datasets of colocated MWR and radiosonde observations taken

415   from two research vessels (RV): the RV Polastern, going through the equator from northern Europe to southern

416   Africa or America in the framework of the OCEANET programme (Griesche et al., 2020), and the RV Meteor,

417   deployed offshore the Barbados in between the Caribbean sea and the Atlantic ocean (Schnitt et al., 2024) in the

418   framework of the EUREC[4]A (Elucidating the Role of Clouds-Circulation Coupling in Climate, Bony et al., 2017)

419   project. Other ship-based MWR deployments exist (e.g., Cimini et al., 2003; Yan et al., 2022) or are currently

420   being collected on a barge within the third Wind Forecast Improvement Project (WFIP3,

421   https://psl.noaa.gov/renewable_energy/wfip3/), but the datasets were not accessible to us at the time of this

422   analysis. More details about the considered datasets are given below, while Table 2 summarises the main

423   information. Note that the considered datasets include observations from three MWR types, covering all the MWR

424   manufacturers identified in Table 1.

425

426   **Table 2:** Main information on the datasets considered in this study.

Dataset short name	Location	Environment	Deployment	Instruments	References

ENA	Graciosa Island, Azores (PT)	Marine, coastal, eastern north Atlantic	Onshore	MP3000-A	ARM, 2013; 2014
MOL	Lindenberg (DE)	Continental, eastern Germany	Onshore	HATPRO	Güldner & Spänkuch, 2001 Vural et al., 2023
SOF	St-Symphorien (FR)	Continental, south west France	Onshore	HATPRO MTP5	Martinet et al., 2020
PIT	Pituffik, Greenland (DK)	Arctic	Onshore	HATPRO	Pace et al., 2017 Pace et al., 2024
POL	Polarstern RV	Open ocean, northern to southern Atlantic	Offshore	HATPRO	Griesche et al., 2020
MET	Meteor RV	Open ocean, tropical	Offshore	HATPRO	Schnitt et al., 2024 Stephan et al., 2021

427

428 **ENA**: The Eastern North Atlantic (ENA) atmospheric observatory is located on Graciosa Island, part of the Azores

429 archipelago in the northeastern Atlantic Ocean west of Portugal. ENA is the newest atmospheric observatory

430 established by the U.S. ARM programme. The ENA observatory is a few hundred metres away from the coastline,

431 at 30 m altitude above mean sea level, and it is exposed to simil-ocean conditions throughout the year. The ENA

432 observatory also belongs to the Global Climate Observing System (GCOS) Reference Upper Air Network

433 (GRUAN), a network of several atmospheric observatories around the world providing reference-quality data for

434 climate benchmarking (Bodeker et al., 2015). ARM operates continuously a MWR (Radiometrics MP-3000 A,

435 see Table 1) and launches daily radiosondes from ENA (ARM, 2013; 2014). The dataset used here extends from

436 December 31st, 2018, to 15th March, 2019, for a total of 138 matchups between MWR and radiosonde

437 observations.

438

439 **MOL**: The Meteorological Observatory Lindenberg – Richard Aßmann Observatory (MOL-RAO) is operated by

440 the German Meteorological Service (Deutscher Wetterdienst, DWD). The MOL-RAO is located in the federal

441 state of Brandenburg in the north-eastern part of Germany, about 50 kilometres south-east of Berlin, 98 metres

442 above mean sea level. The MOL-RAO runs a comprehensive measurement program including all relevant surface

443 remote sensing and in-situ methods for studying solar and terrestrial radiation, interaction processes between the

444 Earth's surface and the atmosphere, and to produce the "Lindenberg Column", a reference dataset for

445 characterising the vertical structure of the atmosphere from the ground up to the stratosphere (e.g., Neisser et al.,

446 2002). The site contributes to all relevant national and international observational programs and initiatives such

447 as for instance the Aerosol, Clouds and Trace Gases Research Infrastructure (ACTRIS, Laj et al., 2024), Cloudnet

448 (Illingworth et al., 2007), the Baseline Surface Radiation Network (BSRN). MOL-RAO also hosts the lead center

449 of GRUAN, launching 4 radiosondes daily. The Lindenberg site provides a database of long-term MWR

450 observations of about 20 years (Güldner & Spänkuch, 2001) and operates currently two MWRs (Radiometrics

451 MP-3000A and RPG HATPRO G5, see Table 1). The dataset used here extends from September 1st, 2020, to 31st

452 December, 2020, for a total of 492 matchups between HATPRO MWR and radiosonde observations.

453

454 **SOF**: The SOuth west FOGs 3D experiment for processes study (SOFOG3D) is an international field campaign

455 directed by Méteo-France to advance our understanding of fog processes at the smallest scale to improve fog

456 forecasts by numerical weather prediction. SOFOG3D lasted from October 2019 to April 2020, during which an

457 unprecedented set of remote sensing and in-situ instruments was deployed during the whole winter period. A

458 unique network of eight MWR, was operated in a 300-by-300 km domain in the South-west of France (Martinet

459 et al., 2020; Martinet et al., 2022) for a better understanding of the spatio-temporal variability of fog at regional

460 scales and to conduct first data assimilation trials (Thomas et al., 2024). Two MWR were operated side-by-side

461 at the super-site, one HATPRO and one MTP5 (see Table 1). The dataset used here extends from 10 November

462 2019 to 12 March 2020, for a total of 61 matchups between two MWR units and radiosonde observations.

463

464 **PIT**: The Thule High Arctic Atmospheric Observatory (THAAO; https://www.thuleatmos-it.it/index.php) is

465 located within the U.S. Pituffik Space Base (formerly known as Thule Air Base) along the north-western coast of

466 Greenland (76,5°N, 68,8°W). The THAAO is on South Mountain, at 220 m above sea level and at about 3 and 11

467 km from the sea and from the Greenland ice sheet, respectively. THAAO is an international facility overseen by

468 the National Science Foundation which took over management in 2017 after the Danish Meteorological Institute

469 (DMI) discontinued their science activities at Pituffik. Research institutions from Italy (ENEA, INGV, University

470 of Roma "La Sapienza", University of Florence) and US (NCAR, AFRL) contribute to THAAO scientific

471 activities. The dataset used here was acquired in the frame of the SVAAP project (Study of the water VApour in

472 the polar AtmosPhere; Meloni et al. 2017) and extends from 12 July 2016 to 21 February 2017, for a total of 35

473 matchups between MWR and radiosonde observations.

474

475 **POL**: The ice breaker RV Polarstern is operated by the Alfred Wegener Institute for Polar and Marine Research

476 (AWI), and typically operates in the Arctic and Antarctic seas (Griesche et al., 2020; Engelmann et al., 2021;

477 Walbröl et al., 2022; and references therein). Atmospheric measurements are conducted en route to collect datasets

478 for investigating the energy budget between ocean and atmosphere and providing ground-truth information for

479 climate models. Continuous observations of aerosol, cloud, temperature and humidity profiles, liquid-water path,

480 solar and thermal radiation, sensible and latent heat are performed. The remote-sensing instruments are hosted in

481 a sea container deployed at the upper deck, starboard of Polarstern at about 22 m above sea level, called the

482   OCEANET platform. OCEANET houses an extensive suite of ground-based remote-sensing instruments,
483   including a multiwavelength Raman polarisation lidar and one 14-channel microwave radiometer (RPG
484   HATPRO, see Table 1). Polarstern also hosts a SCalable Automatic Weather Station (SCAWS), belonging to
485   DWD, which includes a radiosonde launching system. One radiosonde per day is launched routinely from the
486   deck of the Polarstern RV, between 11-12 UTC, but additional launches are occasionally performed earlier or
487   later in the day (e.g., ~09 or 22 UTC). The considered cruises swept the Atlantic Ocean from north to south and
488   return. The dataset used here were collected during sixteen 2-month cruise missions, extending from 20 April
489   2007 to 9 December 2016, for a total of 316 matchups between MWR and radiosonde observations.

490

491   **MET**: The RV Meteor participated in the EUREC[4]A project (Bony et al., 2017; Stevens et al., 2021), a 5-week
492   campaign in the Tropical Atlantic windward and in the close vicinity of Barbados, which included ship-based
493   MWR (Schnitt et al., 2024) and radiosonde (Stephan et al., 2021) observations. During EUREC[4]A (January to
494   February, 2020), MWR measurements aboard the RV Meteor were performed by a HATPRO G5 operated by the
495   Leipzig Institute for Meteorology, so called LIMHAT. The LIMHAT MWR was placed on the navigation deck
496   of the ship at 15.8 m above sea level, operated at a temporal resolution of 1s in zenith mode, with elevation scans
497   performed every full hour. Radiosondes were also launched from the same deck. Before February 9th, radiosondes
498   were launched from the port side of the ship, and after that date, from the stern of the ship due to the failure of the
499   sonde container (Stephan et al, 2021). A linear regression was used to retrieve temperature profiles (Schnitt et al.,
500   2024; Walbröl et al., 2022), trained with a large dataset of daily radiosoundings launched from 1990 until 2018
501   from Grantley Adams International Airport in Barbados (station ID 78954 TBPB). The dataset used here extends
502   from 16 January to 1 March 2020, including 219 radiosondes, providing a total of 145 (68) matchups between
503   radiosonde observations and MWR zenith (elevation scan) retrievals.

504

505   **3.3 Methodology**

506   Following Bianco et al. (2017), the MWR ability to provide atmospheric stability is assessed through the analysis
507   of vertical gradients of atmospheric temperature (dT/dz) and potential temperature (dθ/dz) in the 50-300 m vertical
508   range. Here, the potential temperature profile is calculated using Eq.(2) with P_0=1000 mb and R/c_p=0.286. The
509   profiles of T (in K) and P (in mb) are given by the temperature profile retrieved from the MWR and the pressure
510   profile estimated via the atmospheric thickness equation (with the temperature retrievals and the surface pressure
511   measured by the sensor embedded within the MWR as inputs). For all the datasets we consider radiosondes as
512   reference measurements for atmospheric temperature and potential temperature. Potential temperature from
513   radiosondes is computed as above but using temperature and pressure measurements from the radiosonde sensors.
514   Temporal colocation between MWR measurements and radiosonde data is achieved averaging the MWR

Atmospheric
Measurement
Techniques
Discussions

Open Access

EGU

515   measurements within 30 minutes after the radiosonde launch. For spatial colocation, radiosonde data are

516   interpolated on the vertical grid defined for MWR profile retrievals. Examples of simultaneous MWR and

517   radiosonde profiles for temperature and potential temperature are shown in Figure 8, for two of the considered

518   datasets (ENA and SOF) including the three most common commercially-available MWR types. Figure 8

519   indicates that MWR can generally reproduce the structure of both temperature and potential temperature profiles,

520   although at a lower vertical resolution. Looking at the potential temperature profiles, the two selected cases

521   correspond to classic unstable and neutral/stable atmospheric conditions (Stull, 2012). For each of the available

522   datasets, we produce couplets of T and θ profiles from MWR and radiosonde, from which statistical agreement is

523   computed in terms of vertical profiles of bias, standard deviation (STD), and RMS difference. For each couplet,

524   vertical gradients between 50-300 m are computed (dT/dz and dθ/dz) from both MWR and radiosonde profiles.

525   Figure 9 shows a 2.5-month time series of dθ/dz at ENA site as computed from MWR and radiosondes. The

526   statistical agreement is then computed in terms of mean average (AVG), STD, RMS and maximum absolute error

527   (MAE). Typical uncertainty of radiosonde temperature measurements below 5 km is ~0.2-0.5 K (Dirksen et al.,

528   2014). Thus, assuming uncorrelated uncertainty at different layers, the uncertainty of temperature gradients from

529   radiosonde is estimated as ~1.1-2.8 K/km. However, the representativeness uncertainty, resulting from the

530   representation of an air volume with radiosonde point measurements, is probably dominating and more difficult

531   to estimate generically, as it depends on site climatology and meteorological conditions.

532

533

534
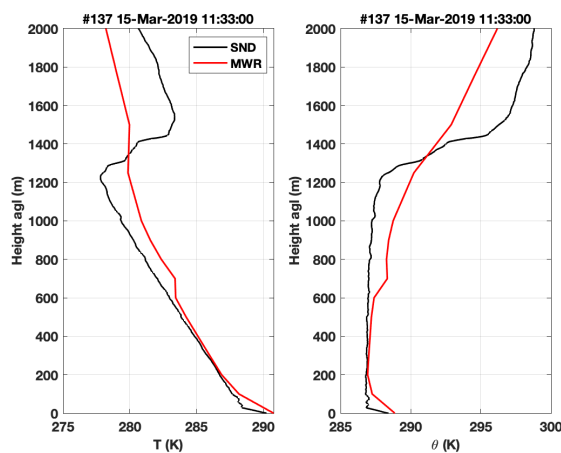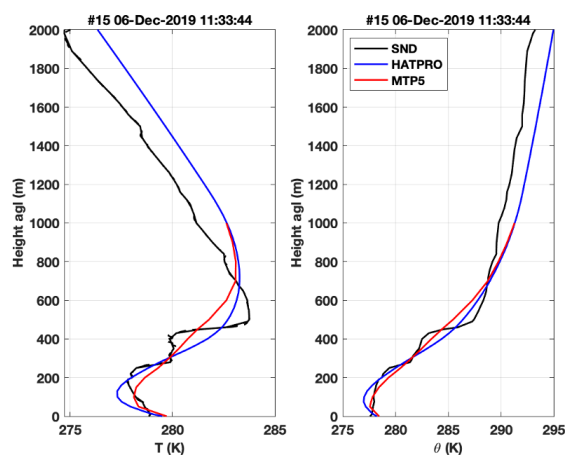
Figure 8: Simultaneous temperature (left) and potential temperature (right) profiles from radiosonde (black) and three MWR

types. Top: MP3000-A (red) at the ENA site (unstable conditions). Bottom: HATPRO (blue) and MTP5 (red) at the

SOFOG3D supersite (neutral to stable conditions). Note that MTP5 retrievals are limited to 1-km height.

538
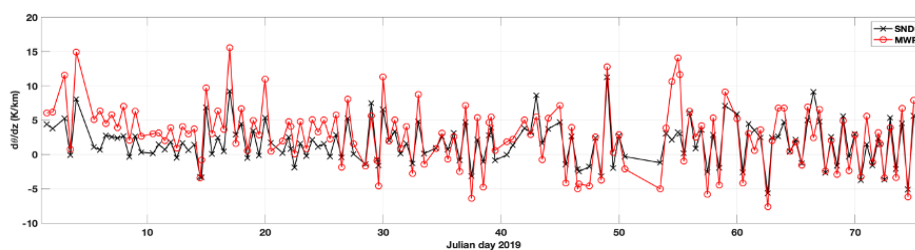
Figure 9: 2.5-month time series of potential temperature lapse rate ($d\theta/dz$) between 0 and 300 m a.g.l. derived from MWR

temperature retrievals (red line) and from radiosonde observations (black line). Dataset from Graciosa Island from 1 January

to 15 March, 2019.

543

4 Validation

This Section presents quantitative results of the statistical analysis on the ability of MWR to provide atmospheric

temperature and potential temperature profiles and vertical gradients, which are related to the atmospheric

stability. The results are discussed below separately for each dataset.

548

23

549 **ENA:** The first considered dataset was collected at the ENA observatory, located a few hundred metres away
550 from the northern coastline of Graciosa Island in the Eastern North Atlantic, conveniently exposed to Atlantic
551 ocean conditions throughout the year. The considered dataset of MWR profiler and radiosonde observations spans
552 about 3 months (from 2019-01-01 to 2019-03-15). The MWR is a Radiometrics MP3000-A (see Table 1). Two
553 radiosondes per day are launched from ENA at ~11:30 and 23:30 UTC, providing 138 matchups between MWR
554 retrievals and radiosonde profiles in the considered period. From the set of 138 matchups, statistics for temperature
555 and potential temperature profile accuracy are calculated. Accordingly, for the ENA dataset Figure 10 reports the
556 vertical profiles of bias, STD, and RMS difference between temperature and potential temperature profiles
557 measured by radiosondes and estimated by MWR. The scores for temperature profile retrievals are in line with
558 those available from the open literature (Cimini et al., 2006; Löhnert and Maier, 2012; Bianco et al., 2017). The
559 scores for potential temperature profiles are very similar to those for temperature profiles, though not exactly the
560 same due to the influence of pressure profile (measured by radiosondes while estimated from surface pressure and
561 retrieved temperature by MWR). Figure 11 reports the scatter plot of temperature gradient (dT/dz) and potential
562 temperature gradient ($d\theta/dz$) in the vertical range (50-300 m). It shows that MWR estimates of either dT/dz or
563 $d\theta/dz$ are correlated with radiosonde measurements throughout the spanned range, with larger scatter towards
564 higher values. The range of $d\theta/dz$ goes from negative to positive values (indicatively from -5 to +15 K/km), i.e.
565 from atmospheric stable through neutral to unstable conditions. The statistical results are computed from the two
566 samples of dT/dz and $d\theta/dz$ couplets in terms of AVG, STD, RMS, and MAE. A summary from all the considered
567 datasets is reported in Table 3. For convenience, Table 3 also reports the statistical results from Bianco et al.
568 (2017), as obtained from the XPIA dataset from Colorado (USA). For the ENA datasets, these can be summarised
569 as follows: for both temperature gradient (dT/dz) and potential temperature gradient ($d\theta/dz$), the MAE results
570 within 2.4 K/km, bias within -1.2 K/km, with 0.72 correlation. These performances are somewhat worse than
571 those reported by Bianco et al. (2017) for XPIA, i.e. MAE within 2.2 K/km, bias within -0.1 K/km, with 0.95
572 correlation. Note that the same MWR type operates at the two sites (MP-3000A), but the notable difference may
573 be related to the status of the instrument calibration and/or the appropriate fitting of the retrieval coefficients to
574 the different climatology conditions (ENA: winter marine environment; XPIA: spring mountain environment).
575

Atmospheric
Measurement
Techniques
Discussions

576
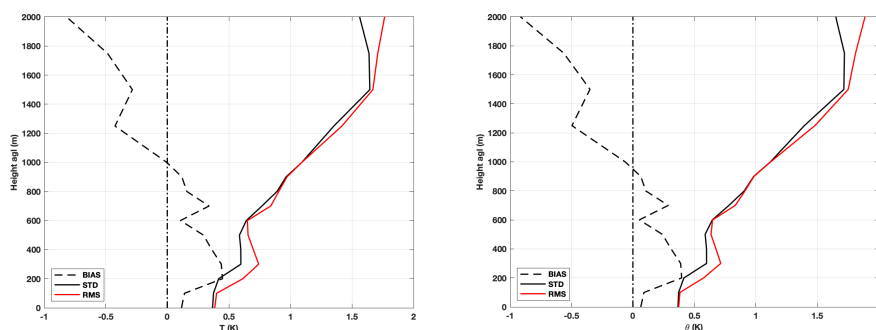
Figure 10: (Left) Bias, standard deviation (STD), and root-mean-square (RMS) differences of the MWR-minus-radiosonde
temperature residuals from the 138 matchups collected at the ENA observatory on Graciosa Island (Eastern North Atlantic)
from 2019-01-01 to 2019-03-15. (Right) Same but for potential temperature profiles.

580
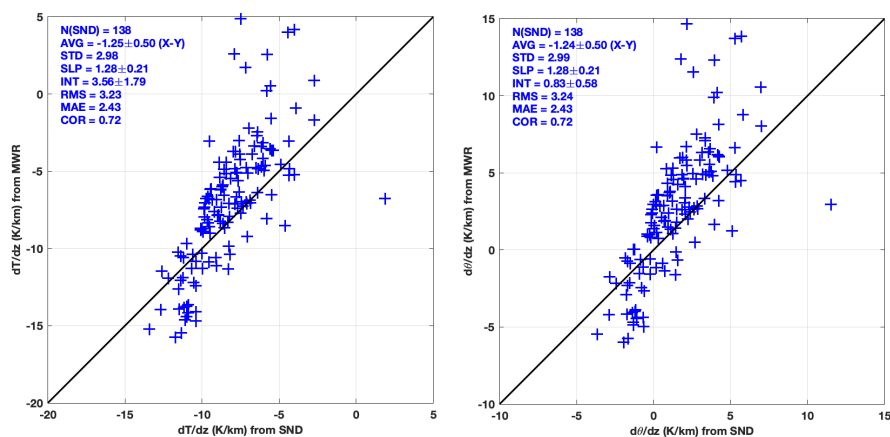
Figure 11: Comparison of atmospheric lapse (50–300 m) for temperature (left) and potential temperature (right) for
MWR retrievals vs. radiosonde measurements collected at the ENA observatory on Graciosa Island from 2019-01-01 to
2019-03-15. Text within each panel as in Figure 5. Units for AVG, STD, RMS, and MAE are in K/km.

585

MOL: This dataset was collected at the MOL in north-eastern Germany, about 98 metres above mean sea level,
characterised by typical mid-latitude continental climatology conditions. The considered dataset of MWR profiler
and radiosonde observations spans about 4 months (from 2020-09-01 to 2020-12-31). The MWR is a RPG Hatpro

25

Atmospheric
Measurement
Techniques
Open Access
Discussions
EGU

589   G5 (see Table 1). Four radiosondes per day are launched at ~5:30, 11:30, 17:30 and 23:30 UTC, providing 492

590   matchups between MWR retrievals and radiosonde profiles. From the set of 492 matchups, statistics for

591   temperature profile accuracy are calculated and reported in Figure 12a, similarly to Figure 10. Also for this dataset,

592   the scores for temperature profile retrievals are in line with those available from the open literature, though the

593   STD/RMS increases more rapidly in the 200-1400 m vertical range. The statistics for the potential temperature

594   profiles are almost identical to those for temperature and thus are not shown for this nor for the remaining datasets.

595   Scatter plots of dT/dz and dθ/dz from MWR and radiosondes are reported in Figure 13a. As for ENA, the MOL

596   dataset corresponds to different climatology (autumn continental environment) with respect to that of XPIA. The

597   behaviour of both dT/dz and dθ/dz are similar for the ENA and MOL sites, though showing higher correlation at

598   MOL (0.91) than at ENA (0.72).

599
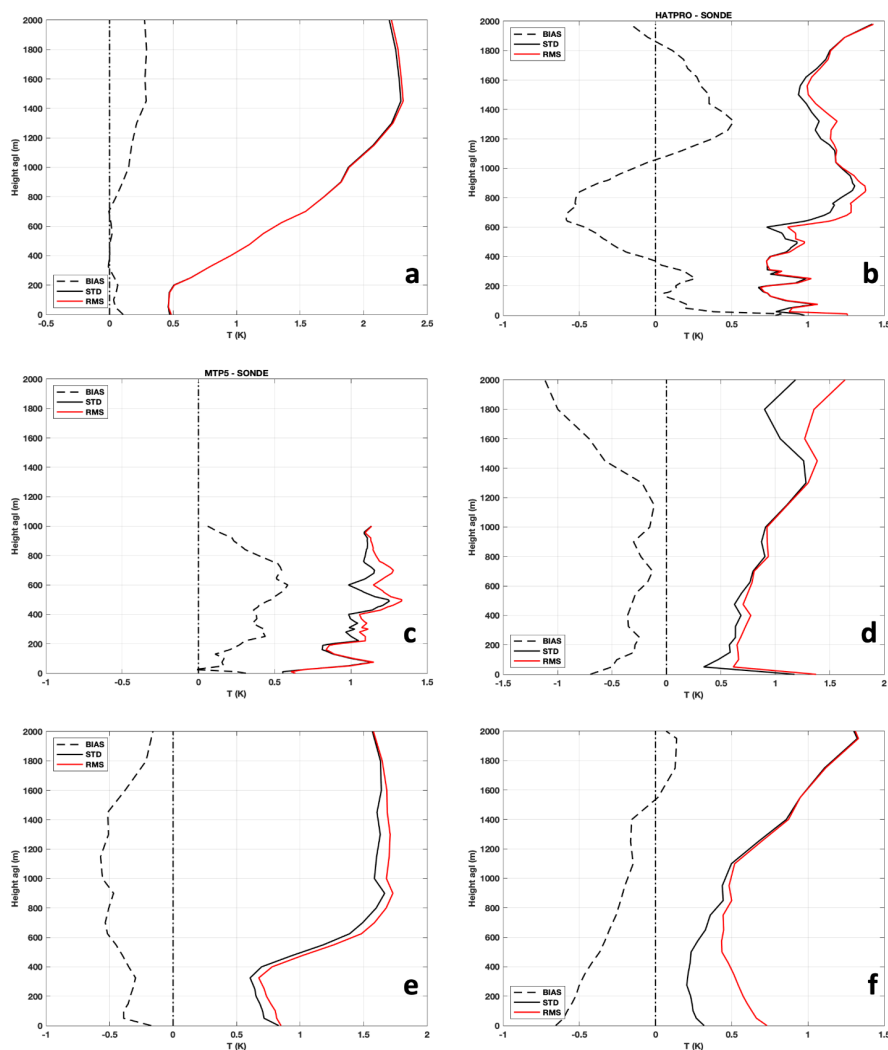
Figure 12: Profiling performances for temperature profiles as in Fig. 8, but obtained from the other considered datasets: (a) 492 matchups collected at MOL (Lindenberg, Germany) from 2020-09-01 to 2020-12-31. (b) 61 matchups during the SOFOG3D campaign (Saint-Symphorien, France, October 2019 to April 2020) for the HATPRO MWR. (c) 61 matchups during the SOFOG3D campaign, but for the MTP-5 MWR (limited to 1 km altitude above ground). (d) 35 matchups during the SVAAP project (2016-07-12 to 2017-02-21) collected at Pituffik (Greenland). (e) 298 matchups from sixteen Polarstern

27

606   RV cruises from 2007 to 2016. (f) 145 matchups from the RV Meteor during the EUREC[4]A campaign (from 2020-01-16 to

607   2020-03-01, zenith-mode only).

608

609
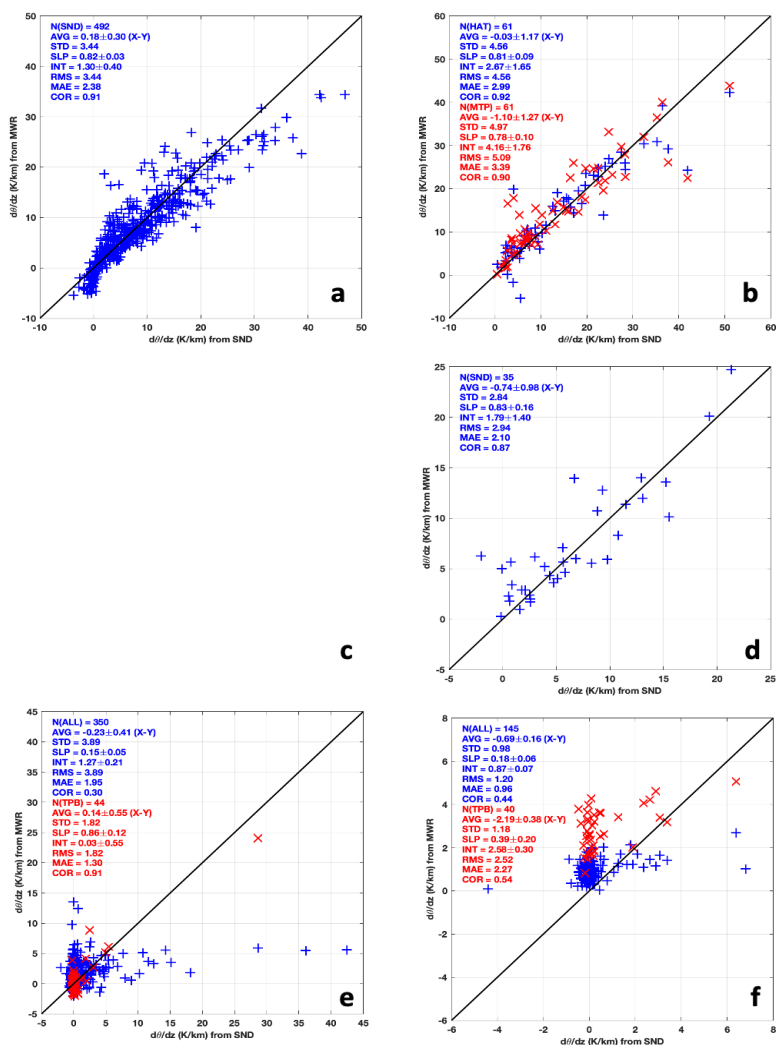
Figure 13: Comparison of atmospheric potential temperature lapse rate as in Fig.9 but for MWR retrievals vs. radiosonde

611   measurements collected at other sites: (a) MOL (Lindenberg, Germany). (b) SOFOG3D campaign (Saint-Symphorien,

Atmospheric
Measurement
Techniques
Discussions

Open Access

EGU

612   France); blue crosses indicate HATPRO data, red Xs indicate MTP-5 data. (c) This panel is left intentionally blank. (d)

613   SVAAP project (Pituffik, Greenland). (e) Polarstern RV cruises (North-South Atlantic); blue crosses indicate all retrieval at

614   zenith, red Xs indicate elevation scan retrievals (2016 only). (f) Meteor RV during EUREC[4]A campaign (Barbados); blue

615   crosses indicate retrievals at zenith, red Xs indicate elevation scan retrievals. Text within each panel as in Figure 5. Units for

616   AVG, STD, RMS, and MAE are in K/km.

618   **SOF:** The same analysis is performed on the dataset collected during the Météo-France SOFOG3D international

619   field campaign in South-west of France. Two MWR were operated side-by-side at the supersite in Saint-

620   Symphorien, one HATPRO and one MTP5 (see Table 1). 61 radiosondes were launched, mostly during stable

621   conditions prone to fog formation during the period from 2019-11-10 to 2020-03-10. Statistical comparison of the

622   61 radiosonde profiles with nearly simultaneous MWR retrievals from both the HATPRO and MTP5 are reported

623   in Figure 12b-c. Note that retrievals from MTP5 are limited to 1 km altitude, while retrievals from HATPRO are

624   provided up to 10 km (although the sensitivity drops to negligible values above 2-3 km). For the vertical range

625   covered by both radiometers (< 1 km), their performances are quite similar (in terms of bias, STD, and RMS),

626   with slightly better performances close to the surface for the MTP5. Statistics for temperature and potential

627   temperature gradients in the 50-300 m vertical range during the SOFOG3D experiment are shown in Figure 13b.

628   As for the temperature profiles, also for the gradients the performances of the two radiometers are quite similar.

629   The HATPRO shows slightly higher scores (e.g, ~2% increase in correlation) than MTP5, despite the slightly

630   better profiling performances of the MTP5 near the surface.

632   **PIT:** This dataset was collected at the THAAO within the U.S. Pituffik space base along the north-western coast

633   of Greenland, at 220 m above sea level, characterised by typical Arctic climatology conditions. The MWR is a

634   RPG Hatpro G2 (see Table 1). During the SVAAP project (2016-07-12 to 2017-02-21), radiosondes were

635   launched sporadically during clear-sky conditions, with a total of 35 matchups between MWR retrievals and

636   radiosonde observations. Statistics for temperature and profile accuracy are calculated and reported in Figure 12d.

637   Also in this case, the scores for temperature profile retrievals are in line with those available from the open

638   literature, though slightly larger than expected near the surface. Figure 13d reports the scatter plot of potential

639   temperature gradient ($d\theta/dz$). This dataset corresponds to yet another climatology (polar environment) with

640   respect to the previous ones. The statistical scores for both dT/dz and $d\theta/dz$ are similar to the previous sites, higher

641   than ENA but slightly lower than MOL/SOF in terms of correlation (~0.87).

643   **POL:** This dataset consists of MWR and radiosonde data from sixteen Polarstern RV cruises (from 2007 to 2016)

644   from northern to southern Atlantic, across the Equator. One radiosonde per day was launched routinely between

645   11-12 UTC, but other launches were performed occasionally. A total of 466 radiosonde launches have been

646   collected during the sixteen cruises, leading to 365 matchups with MWR data, of which 350 survived a quality

647 control screening. From the set of 350 matchups, statistics for temperature profile accuracy are calculated and

648 reported in Figure 12e. The statistics for temperature profile retrievals are larger than those available from the

649 open literature, especially below 500 m. While the systematic component (bias) stays within 0.5 K, the random

650 component (STD) presents a peak near to the surface, leading to ~0.8 K RMS. This feature naturally affects the

651 comparison of temperature and potential temperature gradients. Figure 13e reports the scatter plot of $d\theta/dz$

652 measured by the MWR and the radiosondes, clearly showing low correlation (~0.3). It appears that except for few

653 cases, the radiosondes measure nearly neutral stability (i.e., $d\theta/dz\sim0$ K/km) while the MWR reports all the range

654 from slightly unstable ($d\theta/dz<0$ K/km) to very stable conditions ($d\theta/dz>0$ K/km). In addition, for the few cases

655 in which radiosondes measure very stable conditions ($d\theta/dz>10$ K/km), the MWR retrievals seem to saturate at

656 ~5 K/km. One possible cause may be the zenith-only observation mode adopted during these Polarstern RV

657 cruises. In fact, although elevation scanning observations are proved to increase the accuracy of MWR temperature

658 retrievals (Cimini et al., 2006), especially below 1 km, the zenith-only mode was chosen aboard the Polarstern

659 RV to avoid mispointing problems caused by the ship pitch and roll movements. This cause can be investigated

660 by analysing further the dataset of Polastern RV data collected during the two cruises in 2016, when elevation

661 scanning observations were also available. The analysis of this additional dataset, corresponding to MWR

662 retrievals from elevation scanning observations during the two cruises of 2016, is also reported in Figure 13e.

663 Although the scatter of potential temperature gradients seems similar, the statistical scores of elevation scanning

664 retrievals improve substantially with respect to zenith only, in terms of RMS (from 3.78 to 1.84 K/km), MAE

665 (from 1.97 to 1.30 K/km), and correlation (from 0.31 to 0.90), though the latter is mostly driven by only one point

666 (at 27 K/km). Although limited, this dataset seems to confirm that elevation scanning is indeed desirable for off-

667 shore MWR deployment. Another possible cause of the rather poor performances may be related to the dataset

668 used to train the inversion method (multiple regression). As detailed in Doktorowski (2017), the training is based

669 on a homogenised dataset of 2621 radiosondes launched from cargo vessels in all climatic zones between 60N

670 and 60S, which may be too broad to represent the peculiar environmental conditions encountered by the Polarstern

671 during the sixteen cruises from 2007 to 2016. In particular, the training set may under-represent the deep neutral

672 conditions which seem to characterise most of the radiosonde profiles during the Polarstern RV cruises.

673

674 **MET:** Another ship-based dataset of colocated MWR and radiosonde observations is available from the RV

675 Meteor during the EUREC[4]A project. 219 radiosondes were launched from the RV Meteor between 2020-01-16

676 and 2020-03-01, corresponding to typical tropical conditions. The LIMHAT Level 3 version 2.0 dataset is used

677 here (Schnitt et al, 2023). From this dataset, 145 matchups between radiosonde observations and MWR zenith

678 temperature profile retrievals are available, for which the statistical agreement is calculated and reported in Figure

679 12f. STD for temperature profile retrievals is in line with the expectations from the open literature, while the bias

680 presents a ~0.7 K peak near to the surface, dominating the RMS in the lower 500 m. The scatter plot of potential

681 temperature gradients is reported in Figure 13f, for both the zenith-mode (145 matchups) and elevation-mode
682 retrievals (40 matchups). Similarly to POL, radiosonde data indicate dominant nearly-neutral conditions (dθ/dz~0
683 K/km), while MWR data mostly indicate slightly stable conditions (dθ/dz~0-4 K/km). For the few cases where
684 radiosondes indicate either unstable (dθ/dz~-4 K/km) or stable conditions (dθ/dz~7 K/km), the zenith-mode data
685 remain with 0-3 K/km, resulting in low correlation overall (0.44). Correlation is slightly larger for elevation-mode
686 retrievals (0.54), but also MAE is larger (2.27 K/km) due to a ~3-time larger AVG. Note that, while theory and
687 previous field campaigns have shown that elevation scans should improve the retrieved temperature profiles in
688 the lowest kilometre (Cimini et al. 2006), this is the opposite for the EUREC[4]A LIMHAT dataset. In fact, as
689 reported by Schnitt et al. 2023, bias and RMS for the elevation-mode retrievals increase substantially with respect
690 to zenith-mode (by a factor of 2 near the surface, see their Fig. 9). The authors attribute this to the training set
691 (radiosondes launched from Grantley Adams International Airport), which may be impacted by an island effect,
692 leading to warmer temperatures near the surface compared to the zenith column over the ocean. Another potential
693 reason is the ship pitch and roll movements, since the LIMHAT was not stabilised, which may especially affect
694 observations at low elevation angles.

695

696 **Table 3:** Summary of the statistics for temperature and potential temperature gradients from MWR validated against
697 radiosonde measurements (50-300 m AGL). Note that for XPIA, the correlation coefficient is derived from the coefficient of
698 determination (R^2) given in Bianco et al., 2017. POL(ZNT-ALL) indicates zenith-only MWR retrievals from all 16 Polastern
699 cruises (2007-2016), while POL(ELV-2016) indicates elevation-scan MWR retrievals from two Polastern cruises in 2016.

	Temperature gradients			Potential temperature gradients		
Dataset	**Bias (K/km)**	**MAE (K/km)**	**Correlation**	**Bias (K/km)**	**MAE (K/km)**	**Correlation**
XPIA	0.10	2.10	0.95	0.10	2.20	0.95
ENA	-1.25	2.43	0.72	-1.24	2.43	0.72
MOL	0.16	2.36	0.91	0.18	2.38	0.91
SOF (HATPRO)	0.00	2.97	0.92	-0.01	2.99	0.92
SOF (MTP5)	-1.06	3.37	0.90	-1.10	3.39	0.90
PIT	-0.75	2.06	0.88	-0.74	2.10	0.87
POL(ZNT-ALL)	-0.21	1.93	0.30	-0.23	1.95	0.30
POL(ELV-2016)	0.32	1.42	0.89	0.14	1.30	0.91
MET(ZNT)	-0.59	0.88	0.44	-0.69	0.96	0.44

| MET(ELV) | -2.10 | 2.19 | 0.54 | -2.19 | 2.27 | 0.54 |

700

701   Finally, the scores for temperature and potential temperature gradients from all the datasets, including the

702   reference from Bianco et al. (2017), are reported in Table 3. Note that the range of temperature gradients is quite

703   different in the seven datasets (~30 K/km for XPIA, ~20 K/km for ENA, ~50 K/km for MOL and SOF, ~25 K/km

704   for PIT, ~40 K/km for POL, and ~14 K/km for MET), which affects the values of RMS, MAE, and correlation.

705   The statistics from MOL and SOF (continental mid-latitude sites, winter to spring) are similar, and just slightly

706   lower than those reported for XPIA (mountain site, spring). For the onshore datasets (top six rows in Table 3),

707   potential temperature gradients agree with those from radiosondes with correlation ranging from 0.72 to 0.95 and

708   MAE from 2.10 to 3.39 K/km. The lowest correlation (0.72) corresponds to ENA (winter marine environment),

709   while for all the others correlation is higher than 0.88. This gives some confidence that MWR performances are

710   site independent, provided that the radiometer and inversion method are properly calibrated and trained,

711   respectively. Conversely, the ship-borne datasets (bottom four rows in Table 3) provide substantially lower

712   correlation considering zenith retrievals (0.30 to 0.44). Elevation scanning seems beneficial, increasing correlation

713   (from 0.3 to 0.9 for POL, 0.4 to 0.5 for MET), though for POL is mostly driven by one matchup only and for MET

714   it comes at the expense of ~2-time larger MAE. Note that the MWR retrieval algorithm for the POL and MET

715   datasets is the same (linear regression), though trained with independent datasets (POL: 2621 ship-borne

716   radiosondes; MET: 10871 radiosondes launched from an island-based airport). This suggests that appropriate

717   dedicated training and elevation scanning with ship movement compensation may be required for MWR to catch

718   potential temperature gradients typical of off-shore conditions.

719

720   **5 Summary, conclusions, and outlook**

721   Atmospheric stability is relevant for wind energy applications, as it influences the propagation of wind turbine

722   wakes. Wind turbine rotors operate in the lowest 300 m, and atmospheric stability below and above that height

723   may influence their operations through vertical wind shear and turbulence. Considering different power curves

724   for different stability conditions leads to more accurate and reliable performances of energy production, which

725   lowers the financial risks for both operators and manufacturers. Thus, the ability to model and measure

726   atmospheric stability was reviewed using available datasets of reanalysis and mesoscale NWP model output, tower

727   measurements, and ground-based remote sensing observations.

728   Surface stability metrics from model datasets, including NWP (NEWA and DOWA) and global reanalysis

729   (ERA5), have been assessed against measurements from met masts and floating lidar, focusing on the Obukhov

730   length. The results confirm that when the main drivers of atmospheric stability are correctly characterised by the

Atmospheric
Measurement
Techniques
Discussions

Open Access

EGU

731   bulk formulations used in NWP models, the modelled Obukhov length time series compare to those derived from
732   measurements. Overall, the best match between model data and measurements is observed for ERA5 datasets, in
733   particular computed from the fluxes for unstable conditions and using the bulk Richardson number for stable
734   conditions. Two examples are reported to illustrate how the modelled Obukhov length time series can improve
735   wind-related analyses. The first demonstrates how the atmospheric stability class indicated by the modelled
736   Obukhov length correlates to turbulence intensity and wind speed spectra, both progressively increasing as
737   conditions shift from stable to neutral to unstable. The second example shows that surface-layer expressions, such
738   as Monin-Obukhov Similarity Theory, predict reasonably the wind speed profile in neutral and unstable
739   conditions, while significantly overpredict wind speed measurements in stable conditions, requiring additional
740   information on upper air effects (e.g. the boundary layer height) to better capture the wind speed above 30 m. The
741   ability of NWP models to characterise air temperature profiles in different stability conditions was assessed in the
742   30-100 m vertical range against tower measurements (at FINO1/FINO2 platforms). Both DOWA and NEWA are
743   quite accurate on average, with mean differences of ~0.3-0.5 K with respect to measurements, with no clear pattern
744   with respect to the stability class. Conversely, both DOWA and NEWA models show increased RMS in stable
745   conditions with respect to unstable conditions, with a minimum RMS in neutral conditions. DOWA performs
746   better than NEWA, the first showing RMS within 1 K regardless of stability conditions, while the second showing
747   RMS up to 2.2 K, especially in very stable conditions. Also for temperature gradients in the 50-100 m layer, the
748   DOWA performs better than NEWA, as measured by MAE (3.4-4.0 K/km for DOWA, 3.5-4.2 K/km for NEWA),
749   RMS (5.8-7.3 K/km for DOWA, 6.4-8.4 K/km for NEWA), and correlation (0.77-0.80 for DOWA, 0.70-0.71 for
750   NEWA).

751   Thus, it is concluded that reanalysis and NWP models do provide wind energy practitioners with useful
752   information on atmospheric stability (e.g., Obukhov length) for many situations, i.e., the mean can be used for a
753   range of analyses, including estimates of turbulence and wind shear. However, in specific cases (e.g., elevated
754   temperature inversion) and especially during near-surface stable stratification, the simulated profiles may not be
755   sufficiently accurate. Typical conditions for difficult stability characterization have been illustrated using datasets
756   of surface wind from SAR observations and in situ temperature/wind profiles from UAS measurements. Cases
757   with long wind farm wakes, as they typically occur in a stably stratified ABL, have been identified when
758   observations and models at surface indicate unstable and neutral conditions, suggesting the need for continuous
759   measurements above the height of typical met mast (~100m).

760   This need can be satisfied by nearly continuous observations from ground-based remote sensing atmospheric
761   profilers, and this study addresses the specific question: How good are atmospheric stability retrievals from
762   microwave radiometer measurements for wind energy applications in different climates? Here, the ability of
763   commercially-available MWR to profile atmospheric temperature within the first 2 km and to provide potential

Atmospheric
Measurement
Techniques
Open Access

EGU

Discussions

764 temperature gradients in the vertical range of wind turbine rotors has been assessed against in situ radiosonde

765 measurements. Several sources of MWR data have been identified and analysed, giving preference to datasets in

766 different environments and climatological conditions and datasets with observations from all identified MWR

767 manufacturers. This analysis extends the results in Bianco et al. (2017), obtained for the MP3000A deployed in a

768 continental high-elevation site (~1500 m, Colorado, USA), to other MWR types and environmental conditions. In

769 total, six datasets are considered here, of which four are for onshore and two for offshore environments. The four

770 onshore include marine (east-northern Atlantic), continental (north-eastern Germany; south-west France), and

771 Arctic (Greenland) environments. The two offshore datasets are collected from two research vessels: the Polastern,

772 cruising the Atlantic from northern Europe to southern Africa/America, and the Meteor, deployed off the coast of

773 Barbados in the Caribbean sea. The considered datasets include observations from all the identified commercial

774 MWR types (i.e., HATPRO, MP3000A, MTP5). From the analysis of the six datasets considered in this study, we

775 conclude that:

776

777 1) The statistics for temperature profile retrievals are mostly in line with those available from the open

778 literature, i.e., bias within +/-0.5 K and RMS ~0.5 K near the surface increasing to ~1.5 K at 2 km,

779 although with some exceptions (e.g., higher bias and RMS near the surface for HATPRO in SOF and

780 PIF). Statistics from NWP models in the 30-100m altitude range show similar biases but larger RMS

781 (increasingly larger than 0.5 K from unstable to stable conditions, especially for NEWA).

782 2) For the onshore datasets, potential temperature gradients agree with those from radiosondes with

783 correlation ranging from 0.7 to 0.9 and MAE from 2.1 to 3.4 K/km. This mostly confirms the results of

784 a previous study (Bianco et al., 2017), limited to one onshore dataset and one MWR type. Similar

785 performances from sites in different environments and with different climatology give some confidence

786 that MWR performances can be considered site independent, provided that the radiometer and inversion

787 method are properly calibrated and trained, respectively.

788 3) For the offshore datasets, considering zenith retrievals the MAE is relatively small (0.9 to 1.9 K/km)

789 while the correlation is substantially lower (0.3 to 0.4). The low performances are partially due to the

790 relatively narrow range of potential temperature gradients from radiosondes, indicating prevailing neutral

791 conditions. This poses a question on the datasets used to train the inversion algorithm, as global or

792 onshore datasets may under-represent the prevailing neutral conditions shown by the offshore datasets

793 available here.

794 4) Again for the offshore datasets, elevation scanning seems beneficial, increasing correlation (from 0.3 to

795 0.9 for POL, 0.4 to 0.5 for MET). For POL, elevation scanning also decreases MAE, while for MET

796 MAE increases by a factor ~2, due to a 3-time larger AVE. This may also be related to the training data

797   set, which could be affected by an island effect, but also to the ship movement (pitch and roll), which

798   may have some impact on low-elevation observations.

799   5) Considering all the six datasets, the MAE between MWR and radiosonde temperature (and potential

800   temperature) gradients in the 50-300 m vertical range goes from 0.9 to 3.4 K/km, while the RMS

801   difference from 1.2 to 5.1 K/km. The latter includes the uncertainty of the radiosonde temperature sensor

802   (1.1-2.8 K/km). Considering this, the uncertainty of MWR for temperature and potential temperature

803   gradients in the 50-300 m vertical range is estimated between ~0.5-4.3 K/km.

804   This study indicated the lack of systematic off-shore MWR measurements. Systematic off-shore MWR

805   measurements are needed to enlarge the range of meteorological conditions and to characterise the performances

806   under different stability stratifications. The conclusions above indicate that appropriate dedicated training and

807   elevation scanning (with movement compensation, if ship-based) may be required for MWR to catch potential

808   temperature gradients typical of off-shore conditions. Wind energy practitioners may be interested in learning

809   what instrument is best when and where. To address this properly, we would need to have the different MWR

810   types running at the same time in different environments with the same retrieval method. To our knowledge, no

811   such a dataset is currently available, nor plans to implement such an intercomparison. However, other onshore

812   and offshore MWR observation datasets may be exploited to extend this analysis, characterising performances in

813   other conditions and testing optimization strategies, e.g., in the context of the MiradOR (microwave radiometers

814   for assessing offshore wind resources) project, currently under evaluation. Also, instrument synergy may be

815   exploited to increase vertical resolution of temperature profiles and thus improve retrieval performances of

816   temperature gradients, as shown onshore for combined passive (MWR and IRS) and active (RASS) sensors

817   (Turner and Löhnert, 2021; Bianco et al., 2024), although not all these instruments are practical to be deployed

818   offshore. From the above perspectives, one of the most valuable datasets up to date is the one produced recently

819   by the 3rd Wind Forecast Improvement Project (https://psl.noaa.gov/renewable_energy/wfip3/), including MWR,

820   IRS, and several active instruments deployed over a barge off the coast of southern New England.

821

Competing interests

827

Atmospheric
Measurement
Techniques
Discussions

828 **Author contribution**

829 Conceptualization and funding acquisition: DC, RG, and SF acquired the funding, designed and lead the research.
830 Data curation: CA, AB, CK, PM, GP, BP provided experimental data and performed data curation. Visualization:
831 DC, RG, and AB created the figures. Supervision and validation: SG, EG, STN, and FR oversaw the research
832 activity planning and execution, including mentorship external to the core team. Writing: DC, RG, and SF
833 prepared the manuscript original draft, which was reviewed and edited by all co-authors.

854 **References**

855 Atmospheric Radiation Measurement (ARM) user facility. 2014, updated hourly. Microwave Radiometer Profiler
856   (MWRP). 2019-01-01 to 2019-03-15, Eastern North Atlantic (ENA) Graciosa Island, Azores, Portugal (C1).
857   Compiled by M. Cadeddu. ARM Data Center. Data set accessed 2021-02-25 at
858   http://dx.doi.org/10.5439/1025254.

859 Atmospheric Radiation Measurement (ARM) user facility. 2013, updated hourly. Balloon-Borne Sounding
860   System (SONDEWNPN). 2018-12-31 to 2019-03-16, Eastern North Atlantic (ENA) Graciosa Island,
861   Azores, Portugal (C1). Compiled by E. Keeler and J. Kyrouac. ARM Data Center. Data set accessed 2021-
862   02-25 at http://dx.doi.org/10.5439/1021460.

863 Bärfuss, K., Hankers, R., Bitter, M., Feuerle, T., Schulz, H., Rausch, T., Platis, A., Bange, J., Lampert, A. In-situ
864   airborne measurements of atmospheric and sea surface parameters related to offshore wind parks in the
865   German Bight [dataset publication series]. PANGAEA, https://doi.org/10.1594/PANGAEA.902845, 2019.

866 Bianco, L., Friedrich, K., Wilczak, J. M., Hazen, D., Wolfe, D., Delgado, R., Oncley, S. P., and Lundquist, J. K.:
867   Assessing the accuracy of microwave radiometers and radio acoustic sounding systems for wind energy
868   applications, Atmos. Meas. Tech., 10, 1707–1721, https://doi.org/10.5194/amt-10-1707-2017, 2017.

869 Bianco, L., Adler, B., Bariteau, L., Djalalova, I. V., Myers, T., Pezoa, S., Turner, D. D., and Wilczak, J. M.:
870   Sensitivity of thermodynamic profiles retrieved from ground-based microwave and infrared observations to
871   additional input data from active remote sensing instruments and numerical weather prediction models,
872   Atmos. Meas. Tech., 17, 3933–3948, https://doi.org/10.5194/amt-17-3933-2024, 2024.

873 Bodeker G.E., S. Bojinski, D. Cimini, R.J. Dirksen, M. Haeffelin, J.W. Hannigan, D. Hurst, F. Madonna, M.
874   Maturilli, A.C. Mikalsen, R. Philipona, T. Reale, D.J. Seidel, D.G.H. Tan, P.W. Thorne, H. Vömel, J. Wang,
875   Reference upper-air observations for climate: From concept to reality, Bull. Amer. Meteor. Soc., doi:
876   10.1175/BAMS-D-14-00072.1, March, 2015.

877 Bony, S., Stevens, B., Ament, F., Bigorre, S., Chazette, P., Crewell, S., Delanoë, J., Emanuel, K., Farrell, D.,
878   Flamant, C., Gross, S., Hirsch, L., Karstensen, J., Mayer, B., Nuijens, L., Ruppert, J. H., Sandu, I., Siebesma,
879   P., Speich, S., Szczap, F., Totems, J., Vogel, R., Wendisch, M., and Wirth, M.: EUREC4A: A Field
880   Campaign to Elucidate the Couplings Between Clouds, Convection and Circulation, Surveys in Geophysics,
881   38, 1529–1568, https://doi.org/10.1007/s10712-017-9428-0, 2017.

882 Cadeddu, M. P., Liljegren, J. C., and Turner, D. D.: The Atmospheric radiation measurement (ARM) program
883   network of microwave radiometers: instrumentation, data, and retrievals, Atmos. Meas. Tech., 6, 2359–
884   2372, https://doi.org/10.5194/amt-6-2359-2013, 2013.

885 Cao, Y.; Shi, B.; Zhao, X.; Yang, T.; Min, J. Direct Assimilation of Ground-Based Microwave Radiometer Clear-
886   Sky Radiance Data and Its Impact on the Forecast of Heavy Rainfall. Remote Sens., 15, 4314.
887   https://doi.org/10.3390/ rs15174314, 2023.

888 Caumont O., D. Cimini, U. Löhnert, L. Alados-Arboledas, R. Bleisch, F. Buffa, M. E. Ferrario, A. Haefele, T.
889   Huet, F. Madonna, G. Pace, Assimilation of humidity and temperature observations retrieved from ground-
890   based microwave radiometers into a convective-scale model, Quart. Jour. Roy. Met. Soc.,
891   doi:10.1002/qj.2860, 2016.

892 Cimini, D., Haeffelin, M., Kotthaus, S., Löhnert, U., Martinet, P., O'Connor, E., Walden, C., Collaud Coen, M.,
893   Preissler, J.: Towards the profiling of the atmospheric boundary layer at European scale—introducing the
894   COST Action PROBE. Bull. of Atmos. Sci. & Technol. 1, 23–42, https://doi.org/10.1007/s42865-020-
895   00003-8, 2020.

896 Cimini, D., Rosenkranz, P. W., Tretyakov, M. Y., Koshelev, M. A., and Romano, F.: Uncertainty of atmospheric
897   microwave absorption model: impact on ground-based radiometer simulations and retrievals, Atmos. Chem.
898   Phys., 18, 15231–15259, https://doi.org/10.5194/acp-18-15231-2018, 2018.

899 Cimini, D., Nelson, M., Güldner, J., and Ware, R.: Forecast indices from a ground-based microwave radiometer
900   for operational meteorology, Atmos. Meas. Tech., 8, 315–333, https://doi.org/10.5194/amt-8-315-2015,
901   2015.

902 Cimini, D., Hewison, T. J., Martin, L., Güldner, J., Gaffard, C., and Marzano, F. S.: Temperature and humidity
903   profile retrievals from ground-based microwave radiometers during TUC, Meteorologische Zeitschrift, Vol.
904   15, No. 1, 45-56, doi: 10.1127/0941-2948/2006/0099, 2006.

905 Cimini, D., J. A. Shaw, Y. Han, E. R. Westwater, V. Irisov, V. Leuski, and J. H. Churnside: Air temperature
906   profile and air-sea temperature difference measurements by infrared and microwave scanning radiometers,
907   Radio Science, 38, 3, 8045, doi:10.1029/2002RS002632, 2003.

908 Copernicus Climate Change Service (2021): ERA5 hourly data on single levels from 1940 to present. Copernicus
909   Climate Change Service (C3S) Climate Data Store (CDS), DOI: 10.24381/cds.adbb2d47 (Accessed on 07-
910   MAR-2021)

911 de Montera, L., Berger, H., Husson, R., Appelghem, P., Guerlou, L., and Fragoso, M.: High-resolution offshore
912   wind resource assessment at turbine hub height with Sentinel-1 synthetic aperture radar (SAR) data and
913   machine learning, Wind Energ. Sci., 7, 1441–1453, https://doi.org/10.5194/wes-7-1441-2022, 2022.

914 Dirksen, R. J., Sommer, M., Immler, F. J., Hurst, D. F., Kivi, R., and Vömel, H.: Reference quality upper-air
915   measurements: GRUAN data processing for the Vaisala RS92 radiosonde, Atmos. Meas. Tech., 7, 4463–
916   4490, https://doi.org/10.5194/amt-7-4463-2014, 2014.

917 Doktorowski, T., Improvement of retrieval algorithms for determining temperature profiles over the Atlantic,
918   Master Thesis, Leipzig Institute for Meteorology University of Leipzig, February 2017.

919 DOWA, Dutch Offshore Wind Atlass [website], www.dutchoffshorewindatlas.nl/ (last access: 07 March 2021),
920   2021.

921 Engelmann, R., Ansmann, A., Ohneiser, K., Griesche, H., Radenz, M., Hofer, J., Althausen, D., Dahlke, S.,
922   Maturilli, M., Veselovskii, I., Jimenez, C., Wiesen, R., Baars, H., Bühl, J., Gebauer, H., Haarig, M., Seifert,
923   P., Wandinger, U., and Macke, A.: Wildfire smoke, Arctic haze, and aerosol effects on mixed-phase and
924   cirrus clouds over the North Pole region during MOSAiC: an introduction, Atmos. Chem. Phys., 21, 13397–
925   13423, https://doi.org/10.5194/acp-21-13397-2021, 2021.

926 Feltz, W. F., Smith, W. L., Howell, H. B., Knuteson, R. O., Woolf, H., & Revercomb, H. E., Near-Continuous
927   Profiling of Temperature, Moisture, and Atmospheric Stability Using the Atmospheric Emitted Radiance
928   Interferometer (AERI), Journal of Applied Meteorology, 42(5), 584-597. Retrieved Mar 10, 2022, from
929   https://journals.ametsoc.org/view/journals/apme/42/5/1520-0450_2003_042_0584_npotma_2.0.co_2.xml,
930   2003.

931 Grachev, A. A., & Fairall, C. W., Dependence of the Monin–Obukhov Stability Parameter on the Bulk Richardson
932   Number over the Ocean, Journal of Applied Meteorology, 36(4), 406-414, 1997.

933 Griesche, H. J., Seifert, P., Ansmann, A., Baars, H., Barrientos Velasco, C., Bühl, J., Engelmann, R., Radenz, M.,
934   Zhenping, Y., and Macke, A.: Application of the shipborne remote sensing supersite OCEANET for
935   profiling of Arctic aerosols and clouds during *Polarstern* cruise PS106, Atmos. Meas. Tech., 13, 5335–
936   5358, https://doi.org/10.5194/amt-13-5335-2020, 2020.

937 Gryning, SE., Batchvarova, E., Brümmer, B. et al. On the extension of the wind profile over homogeneous terrain
938   beyond the surface boundary layer. Boundary-Layer Meteorol 124, 251–268,
939   https://doi.org/10.1007/s10546-007-9166-9, 2007.

940 Güldner J. and D. Spänkuch, Remote Sensing of the Thermodynamic State of the Atmospheric Boundary Layer
941   by Ground-Based Microwave Radiometry, J. Atmos. Oceanic Technol., 18, 925-933, **18**, 925–933,
942   https://doi.org/10.1175/1520-0426(2001)018<0925:RSOTTS>2.0.CO;2, 2001.

943 Hansen, K.S., Barthelmie, R.J., Jensen, L.E. and Sommer, A., The impact of turbulence intensity and atmospheric
944   stability on power deficits due to wind turbine wakes at Horns Rev wind farm. Wind Energ., 15: 183-196.
945   https://doi.org/10.1002/we.512, 2012.

946 Hersbach, H, Bell, B, Berrisford, P, et al., The ERA5 global reanalysis. Q J R Meteorol Soc. 146: 1999– 2049.
947   https://doi.org/10.1002/qj.3803, 2020.

948 Hervo M., Romanens G., Martucci G., Weusthoff T., Haefele A., Evaluation of an Automatic Meteorological
949   Drone Based on a 6-Month Measurement Campaign. Atmosphere, 14(9):1382.
950   https://doi.org/10.3390/atmos14091382, 2023.

951 Illingworth, A. J., and Coauthors, CloudNet: Continuous evaluations of cloud profiles in seven operational models
952   using ground-based observations. Bull. Amer. Meteor. Soc., 88, 883–898, http://doi:10.1175/BAMS-88-6-
953   883, 2007.

954 Laj, P., and Coauthors, 2024: Aerosol, Clouds and Trace Gases Research Infrastructure (ACTRIS): The European
955   Research Infrastructure Supporting Atmospheric Science. Bull. Amer. Meteor. Soc., 105, E1098–E1136,
956   https://doi.org/10.1175/BAMS-D-23-0064.1.

957 Lin, H., J. Sun, T. M. Weckwerth, E. Joseph, and J. Kay, Assimilation of New York State Mesonet Surface and
958   Profiler Data for the 21 June 2021 Convective Event. Mon. Wea. Rev., 151, 485–507,
959   https://doi.org/10.1175/MWR-D-22-0136.1, 2023.

960 Löhnert, U. and Maier, O.: Operational profiling of temperature using ground-based microwave radiometry at
961   Payerne: prospects and challenges, Atmos. Meas. Tech., 5, 1121–1134, https://doi.org/10.5194/amt-5-1121-
962   2012, 2012.

963 Lundtang Petersen E., Troen I., Ejsing Jørgensen H., Mann J., The new European wind atlas, Energy Bulletin,
964   No. 17, 2014, p. 34-39, https://findit.dtu.dk/en/catalog/545a3b7565e560f358000074

965 Madonna, F., R. Kivi, J.-C. Dupont, B. Ingleby, M. Fujiwara, G. Romanens, M. Hernandez, X. Calbet, M. Rosoldi,
966   A. Giunta, T. Karppinen, M. Iwabuchi, S. Hoshino, C. von Rohden, and P. W. Thorne, Use of automatic
967   radiosonde launchers to measure temperature and humidity profiles from the GRUAN perspective,
968   Atmospheric Measurement Techniques, 13, 3621–3649, doi: 10.5194/amt-13-3621-2020, 2020.

969 Martinet, P., Cimini, D., De Angelis, F., Canut, G., Unger, V., Guillot, R., Tzanos, D., and Paci, A.: Combining
970   ground-based microwave radiometer and the AROME convective scale model through 1DVAR retrievals
971   in complex terrain: an Alpine valley case study, Atmos. Meas. Tech., 10, 3385–3402,
972   https://doi.org/10.5194/amt-10-3385-2017, 2017.

973 Martinet, P., Cimini, D., Burnet, F., Ménétrier, B., Michel, Y., and Unger, V.: Improvement of numerical weather
974   prediction model analysis during fog conditions through the assimilation of ground-based microwave
975   radiometer observations: a 1D-Var study, Atmos. Meas. Tech., 13, 6593–6611, https://doi.org/10.5194/amt-
976   13-6593-2020, 2020.

977 Meloni, D., Di Iorio, T., di Sarra, A. Iaccarino, A., Pace, G., Mevi, G., Muscari, G., Cacciani. and M, Gröbner, J.;
978   The July 2016 Study of the water VApour in the polar AtmosPhere (SVAAP) campaign at Thule,
979   Greenland: surface radiation budget and role of clouds, 19th EGU General Assembly, EGU2017,
980   proceedings from the conference held 23-28 April, 2017 in Vienna, Austria., p.8921,
981   https://meetingorganizer.copernicus.org/EGU2017/EGU2017-8921-1.pdf, 2017.

982 Neisser, J., Adam, W., Beyrich, F., Leiterer, U., and Steinhagen, H., Atmospheric boundary layer monitoring at
983   the Meteorological Observatory Lindenberg as a part of the "Lindenberg Column": Facilities and selected
984   results, metz, 11, 241–253, https://doi.org/10.1127/0941-2948/2002/0011-0241, 2002.

985 NEWA, New European Wind Atlas [website], http://www.neweuropeanwindatlas.eu/ (last access: 07 March
986   2021), 2021.

987 Pace, G., Di Iorio, T., di Sarra, A., Iaccarino, A., Meloni, D., Mevi, G., Muscari, G., and Cacciani M., Microwave
988   measurements of temperature profiles, integrated water vapour, and liquid water path at Thule Air Base,
989   Greenland, 19th EGU General Assembly, EGU2017, proceedings from the conference held 23-28 April,

Atmospheric
Measurement
Techniques

Discussions

990   2017 in Vienna, Austria., p.10226, https://meetingorganizer.copernicus.org/EGU2017/EGU2017-10226-
991   1.pdf, 2017.

992   Pace, G., di Sarra, A., Cali Quaglia, F., Ciardini, V., Di Iorio, T., Iaccarino, A., Meloni., M., Muscari, G., and
993   Scarchilli, C., Verification of parametrizations for clear sky downwelling longwave irradiance in the Arctic,
994   Atmos. Meas. Tech., 17, 1617-1632, https://doi.org/10.5194/amt-17-1617-2024, 2024.

995   Peña, A., Gryning, SE. and Hasager, C.B., Measurements and Modelling of the Wind Speed Profile in the Marine
996   Atmospheric Boundary Layer. Boundary-Layer Meteorol 129, 479–495, https://doi.org/10.1007/s10546-
997   008-9323-9, 2008.

998   Peña, A. and Hahmann, A.N., Atmospheric stability and turbulence fluxes at Horns Rev—an intercomparison of
999   sonic, bulk and WRF model data. Wind Energ., 15: 717-731. https://doi.org/10.1002/we.500, 2012.

1000 Pérez, C., Rivero, M., Escalante, M., Ramirez, V., Guilbert, D.: Influence of Atmospheric Stability on Wind
1001   Turbine Energy Production: A Case Study of the Coastal Region of Yucatan. Energies, 16, 4134.
1002   https://doi.org/10.3390/en16104134, 2023.

1003 Platis, A., J. Bange, K. Barfuss, B. Canadillas, M. Hundhausen, B. Djath, A. Lampert, J. Schulz-Stellenfleth, S.
1004   Siedersleben, T. Neumann, and S. Emeis, Long-range modifications of the wind field by offshore wind
1005   parks – results of the project WIPAFF. Meteorologische Zeitschrift, 29, 5, 355-376, 11,
1006   http://dx.doi.org/10.1127/metz/2020/1023, 2020.

1007 Pinto, J. O., and Coauthors: The Status and Future of Small Uncrewed Aircraft Systems (UAS) in Operational
1008   Meteorology. Bull. Amer. Meteor. Soc., 102, E2121–E2136, https://doi.org/10.1175/BAMS-D-20-0138.1,
1009   2021.

1010 Rüfenacht, R., Haefele, A., Pospichal, B., Cimini, D., Bircher-Adrot, S., Turp, M., Sugier., J,. EUMETNET opens
1011   to microwave radiometers for operational thermodynamical profiling in Europe. Bull. of Atmos. Sci.&
1012   Technol. 2, 4, https://doi.org/10.1007/s42865-021-00033-w, 2021.

1013 Sandu, I., A. Beljaars, P. Bechtold, T. Mauritsen, and G. Balsamo, Why is it so difficult to represent stably
1014   stratified conditions in numerical weather prediction (NWP) models?, J. Adv. Model. Earth Syst., 5, 117–
1015   133, doi:10.1002/jame.20013, 2013.

1016 Sathe, A., Gryning, S.-E. and Peña, A., Comparison of the atmospheric stability and wind profiles at two wind
1017   farm sites over a long marine fetch in the North Sea. Wind Energ., 14: 767-780.
1018   https://doi.org/10.1002/we.456, 2011.

1019 Schnitt, S., Foth, A., Kalesse-Los, H., Mech, M., Acquistapace, C., Jansen, F., Löhnert, U., Pospichal, B.,
1020   Röttenbacher, J., Crewell, S., and Stevens, B.: Ground- and ship-based microwave radiometer
1021   measurements during EUREC4A, Earth Syst. Sci. Data, 16, 681–700, https://doi.org/10.5194/essd-16-681-
1022   2024, 2024.

1023 Schnitt, S., Foth, A., Kalesse-Los, H., Mech, M. & Acquistapace, C., Ground- and ship-based microwave
1024   radiometer measurements during EUREC4A. [dataset]. Aeris. https://doi.org/10.25326/454, 2023.

1025 Shaw, W. J., and Coauthors, The Second Wind Forecast Improvement Project (WFIP2): General overview. Bull.
1026   Amer. Meteor. Soc., 100, 1687–1699, https://doi.org/10.1175/BAMS-D-18-0036.1, 2019.

1027 Shrestha, B., J. A. Brotzge, J. Wang, N. Bain, C. D. Thorncroft, E. Joseph, J. Freedman, and S. Perez: Overview
1028   and Applications of the New York State Mesonet Profiler Network. J. Appl. Meteor. Climatol., 60, 1591–
1029   1611, https://doi.org/10.1175/JAMC-D-21-0104.1, 2021.

1030 Spiridonov V., and Ćurić M., Atmospheric Stability. In: Fundamentals of Meteorology. Springer, Cham. Online
1031   ISBN 978-3-030-52655-9, https://doi.org/10.1007/978-3-030-52655-9_9, 2021.

1032 Stephan, C. C., Schnitt, S., Schulz, H., Bellenger, H., de Szoeke, S. P., Acquistapace, C., Baier, K., Dauhut, T.,
1033   Laxenaire, R., Morfa-Avalos, Y., Person, R., Quiñones Meléndez, E., Bagheri, G., Böck, T., Daley, A.,
1034   Güttler, J., Helfer, K. C., Los, S. A., Neuberger, A., Röttenbacher, J., Raeke, A., Ringel, M., Ritschel, M.,
1035   Sadoulet, P., Schirmacher, I., Stolla, M. K., Wright, E., Charpentier, B., Doerenbecher, A., Wilson, R.,

Jansen, F., Kinne, S., Reverdin, G., Speich, S., Bony, S., and Stevens, B.: Ship- and island-based atmospheric soundings from the 2020 EUREC4A field campaign, Earth System Science Data, 13, 491–514, https://doi.org/https://doi.org/10.5194/essd-13-491-2021, 2021.

Stevens, B. et al., EUREC4A, Earth System Science Data, 13, 4067–4119, https://doi.org/10.5194/essd-13-4067-2021, 2021.

St. Martin, C. M., Lundquist, J. K., Clifton, A., Poulos, G. S., and Schreck, S. J.: Wind turbine power production and annual energy production depend on atmospheric stability and turbulence, Wind Energ. Sci., 1, 221–236, https://doi.org/10.5194/wes-1-221-2016, 2016.

Stull, R. Practical Meteorology: An Algebra-based Survey of Atmospheric Science, version 1.02b. Univ. of British Columbia. 940 pages, ISBN 978-0-88865-283-6, https://www.eoas.ubc.ca/books/Practical_Meteorology/, 2017. Accessed 2021-12-16.

Stull, R.B., An introduction to boundary layer meteorology, volume 13. – Springer Science & Business Media, ISBN 978-90-277-2768-8, https://doi.org/10.1007/978-94-009-3027-8, 2012.

Thomas G., P. Martinet, P. Brousseau, P. Chambon, J-F. Georgis, M. Hervo, T. Huet, U. Löhnert, E. Orlandi, V. Unger : Assimilation of ground-based microwave radiometer temperature observations into a convective-scale NWP model for fog forecast improvement, Quart. J. Roy. Meteor. Soc., in press, 2024.

Turner, D. D. and Löhnert, U.: Ground-based temperature and humidity profiling: combining active and passive remote sensors, Atmos. Meas. Tech., 14, 3033–3048, https://doi.org/10.5194/amt-14-3033-2021, 2021.

Vanderwende, B. and Lundquist, J. K., The modification of wind turbine performance by statistically distinct atmospheric regimes, Environ. Res. Lett., 7, 1–7, doi:10.1088/1748- 9326/7/3/034035, 2012.

Vural, J., Merker, C., Löffler, M., Leuenberger, D., Schraff, C., Stiller, O., Schomburg, A., Knist, C., Haefele, A. and Hervo, M., Improving the representation of the atmospheric boundary layer by direct assimilation of ground-based microwave radiometer observations. Q J R Meteorol Soc. 150(759), 1012–1028, https://doi.org/10.1002/qj.4634, 2023.

Yan H., Y. Zhao, and S. Chen, An Improved 1D-VAR Retrieval Algorithm of Temperature Profiles from an Ocean-Based Microwave Radiometer, Journal of Marine Science and Engineering 10, 5: 641. https://doi.org/10.3390/jmse10050641, 2022.

Wagner, T. J., A. C. Czarnetzki, M. Christiansen, R. B. Pierce, C. O. Stanier, A. F. Dickens, and E. W. Eloranta: Observations of the Development and Vertical Structure of the Lake-Breeze Circulation during the 2017 Lake Michigan Ozone Study. J. Atmos. Sci., 79, 1005–1020, https://doi.org/10.1175/JAS-D-20-0297.1, 2022.

Wijnant, I. L., van Ulft, B., van Stratum, B. J. H., Barkmeijer, J., Onvlee, J., de Valk, S., et al. (2019). The Dutch offshore wind atlas (DOWA): description of the dataset, KNMI Technical report TR-380, Retrieved from https://www.dutchoffshorewindatlas.nl/publications (last access 23 August 2024): https://www.dutchoffshorewindatlas.nl/binaries/dowa/documenten/reports/2019/12/05/knmi-report---dowa-dataset/The+Dutch+Offshore+Wind+Atlas+%28DOWA%29_description+of+the+dataset.pdf

Wilczak, J. M., and Coauthors, The Wind Forecast Improvement Project (WFIP): A public–private partnership addressing wind energy forecast needs. Bull. Amer. Meteor. Soc., 96, 1699–1718, https://doi.org/10.1175/BAMS-D-14-00107.1, 2015.

Wilczak, J. M., and Coauthors, The Second Wind Forecast Improvement Project (WFIP2): Observational Field Campaign. Bull. Amer. Meteor. Soc., 100, 1701–1723, https://doi.org/10.1175/BAMS-D-18-0035.1, 2019.

Wolfe, D. E., and R. J. Lataitis: Boulder Atmospheric Observatory: 1977–2016: The End of an Era and Lessons Learned. Bull. Amer. Meteor. Soc., 99, 1345–1358, https://doi.org/10.1175/BAMS-D-17-0054.1, 2018.

Atmospheric
Measurement
Techniques
Discussions

Open Access

1079   Walbröl, A., Crewell, S., Engelmann, R., Orlandi, E., Griesche, H., Radenz, M., Hofer, J., Althausen, D., Maturilli,
1080   M., and Ebell, K.: Atmospheric temperature, water vapour and liquid water path from two microwave
1081   radiometers during MOSAiC, Scientific Data, 9, 534, https://doi.org/10.1038/s41597-022-01504-1, 2022.

1082